magnetism

MDPI

Review

Unraveling the Magnetic Properties of NiO Nanoparticles: From Synthesis to Nanostructure

Carlos Moya [1,2,*], Jorge Ara [3], Amílcar Labarta [2,3] and Xavier Batlle [2,3]

[1] Departament de Química Inorgànica i Orgànica, Universitat de Barcelona, Martí i Franquès, 1-11, 08028 Barcelona, Spain
[2] Institut de Nanociència i Nanotecnologia (IN2UB), Universitat de Barcelona, 08028 Barcelona, Spain; amilcar.labarta@ub.edu (A.L.); xavierbatlle@ub.edu (X.B.)
[3] Departament de Física de la Matèria Condensada, Martí i Franquès 1, 08028 Barcelona, Spain
* Correspondence: carlosmoyaalvarez@ub.edu

Abstract: NiO nanoparticles have garnered significant interest due to their diverse applications and unique properties, which differ markedly from their bulk counterparts. NiO nanoparticles are p-type semiconductors with a wide bandgap, high discharge capacity, and high carrier density, making them ideal for use in batteries, sensors, and catalysts. Their ability to generate reactive oxygen species also imparts disinfectant and antibiotic properties. Additionally, the higher Néel temperature of NiO compared with other antiferromagnetic materials makes it suitable for high-temperature applications in spintronic devices and industrial settings. This review focuses on the critical role of structure and composition in determining the magnetic properties of NiO nanoparticles. It examines how finite-size surface effects, morphology, crystallinity, and nickel distribution influence these properties. Fundamental physical properties and characterization techniques are discussed first. Various synthesis methods and their impact on NiO nanoparticle properties are then explored. Their magnetic phenomenology is examined in detail, highlighting the effects of finite size, particle composition and surface, and crystal quality. The review concludes with a summary of key insights and future research directions for optimizing NiO nanoparticles in technological applications.

Keywords: antiferromagnetic nanoparticles; nickel oxide nanoparticles; finite-size effects; surface effects; crystallographic properties; magnetic anisotropy; Néel temperature; chemical synthesis methods

Citation: Moya, C.; Ara, J.; Labarta, A.; Batlle, X. Unraveling the Magnetic Properties of NiO Nanoparticles: From Synthesis to Nanostructure. *Magnetism* **2024**, *4*, 252–280. https://doi.org/10.3390/magnetism4030017

Academic Editor: Gerardo F. Goya

Received: 29 June 2024
Revised: 31 July 2024
Accepted: 12 August 2024
Published: 28 August 2024

1. Introduction

Antiferromagnetic (AFM) materials represent a fascinating type of magnetic system, sharing some characteristics with their ferromagnetic (FM) counterparts [1–6]. For example, they both exhibit the formation of magnetic domains due to the cooperative magnetic behavior of the electronic spins within the crystal lattice. In AFM materials, spins align in two sublattices with opposite directions to minimize the system's overall energy, allowing for complex interactions that influence magnetic and electronic properties.

Nickel oxide nanoparticles (NiO NPs) have gained significant interest in AFM materials research due to their size-dependent properties and diverse applications (see Figure 1) [7–9]. NiO NPs are cost-effective and easy to produce and isolate, while still possessing valuable chemical and physical characteristics [7–9]. For instance, they are p-type semiconductors with a wide bandgap (3.6–4 eV) [10,11], high discharge capacity (638 mAh/g) [12], and high carrier density (~$7.35 \cdot 10^{18}$ cm^{-3}) [13]. These properties lead to superior electrochemical performance compared with traditional cathode materials, making them ideal for batteries [12,14–17]. Additionally, the porous nature of nanosized NiO NPs allows them to function as both sensors and catalysts [18]. They can detect relevant compounds, such as ethanol, and catalyze CO oxidation reactions [19–22]. Interestingly, NiO NPs also exhibit disinfectant and antibiotic properties by generating reactive oxygen species that damage microbial cell walls [23–25].

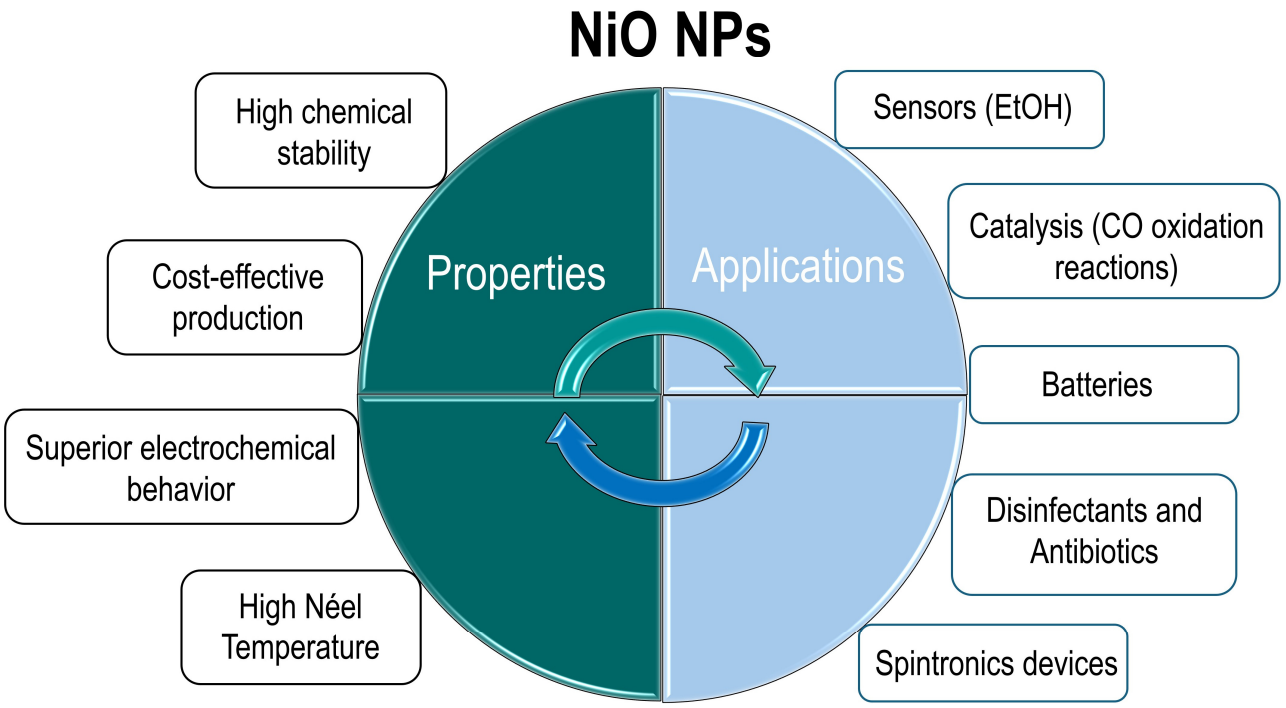

Figure 1. Properties and applications of NiO NPs. The left side shows the inherent properties of NiO NPs, emphasizing their high chemical stability, cost-effective production, superior electrochemical behavior, and high Néel temperature. The right side shows the practical applications of NiO NPs showcasing their utility in ethanol sensing, catalysis of CO oxidation reactions, components in batteries, disinfectants and antibiotics, and use in spintronic devices.

Furthermore, NiO NPs have the highest Néel temperature (T_N = 525 K) among metal monoxides (e.g., FeO, CoO, MnO) [1], making them suitable for applications requiring magnetic stability at elevated temperatures. This is especially valuable in industrial settings where materials experience high heat exposure. As an AFM layer in spintronic devices, NiO maintains AFM order even at higher operational temperatures, enhancing reliability and performance. Moreover, NiO-based sensors can function effectively at higher temperatures compared with those made from materials with lower T_N [26–29].

In bulk NiO, neighboring nickel spins align antiparallel, demonstrating AFM behavior [1–8]. However, when reduced to the nanoscale, surface and finite-size effects start to dominate, often resulting in a nonzero magnetic moment in NiO NPs. This exotic behavior has been studied for decades, beginning with the pioneering investigations by Néel [30], who suggested that the weak FM behavior in these systems could be due to incomplete compensation between the two AFM sublattices. In the 1990s, Kodama et al. proposed that the anomalous magnetic properties observed in these systems could not be fully explained by the two-sub-lattice AFM ordering observed in bulk NiO [31]. Instead, they suggested the emergence of more complex sublattice configurations within the NP due to finite-size effects associated with the size perturbation of the magnetic correlation in each of the two sublattices of the bulk AFM. Subsequent research has extensively examined the impact of finite-size and surface effects on the magnetic properties of NiO NPs, focusing on factors such as particle size, crystal domain boundaries, and Ni oxidation state.

The synthesis routes for synthesizing NiO NPs are crucial in determining their ultimate physical and chemical characteristics [7–9]. These methods range from traditional chemical precipitation to advanced techniques such as sol–gel [32–34], hydrothermal synthesis [35], and thermal decomposition [36,37], each with unique advantages and influencing factors on the NPs' properties. The choice of a synthesis route directly impacts the size, shape, crystallinity, and surface characteristics of NiO NPs, which in turn, affects their electronic, magnetic, and catalytic behaviors. Understanding the synthesis of NiO NPs is not just

about producing these particles but also about tailoring them for specific applications by manipulating their intrinsic properties through controlled fabrication processes. This critical link between the synthesis methods and the properties of NiO NPs underscores the importance of exploring these routes in depth, as it enables the development of NiO NPs with desired functionalities for various applications, from electronics and catalysis to biomedicine and environmental remediation.

This short review aims to shed light on the complex interplay between the crystal structure and the finite-size effects on the magnetic nature of NiO NPs, offering substantial knowledge beneficial to both scientific inquiry and technological advancement. This review is structured into several comprehensive sections, each focusing on a different aspect of NiO NPs. Thus, the second section focuses on the fundamental physical properties of NiO NPs and the primary physicochemical characterization techniques used to understand these properties. The third section explores the synthesis of NiO NPs, emphasizing the influence of crucial parameters such as reagent concentrations and solvents on the morphology and crystallinity of the particles. The fourth section summarizes the magnetic phenomenology of these systems detailing the impact of finite-size and surface effects, particle composition, and crystal quality on the magnetic properties of NiO NPs. Finally, this review concludes with a comprehensive summary and offers a critical perspective on the field, highlighting future research directions and potential applications of NiO NPs.

2. Structural and Magnetic Properties of NiO NPs: Analysis and Characterization Techniques

2.1. Structure vs. Magnetism in NiO NPs

NiO has a face-centered cubic (FCC) atomic arrangement, in which each Ni^{2+} atom is surrounded by six O^{2-} atoms in an octahedral geometry [7–9]. The space group is Fm3m, which renders a lattice parameter of 4.19 Å, and a density of 6.76 g/cm^3 (see Table 1 and Figure 2) [38,39]. Generally, stoichiometric NiO NPs exhibit a pale green color. However, minor changes in the Ni^{2+} oxidation state can result in samples that turn black. Such variations in the crystal structure can promote new energy levels in the band gap, modifying the optical and electronic properties of the material.

Table 1. Key crystal and magnetic features of NiO, such as crystal structure, lattice parameters, unit cell volume, density, magnetic moment per atom, and T_N.

Property	Value
Crystal structure	Cubic (FCC)
Symbol	Fm3m
Length a = b = c (Å)	4.19
Unit cell volume ($Å^3$)	73.37
Density ($g{\cdot}cm^{-3}$)	6.76
μ_{NiO} (μB)	2
T_N (K)	525

NiO is a type-II AFM with a collinear spin structure. The AFM superexchange interaction between Ni ions through oxygen (Ni-O-Ni) bonds along the 100 directions yields FM ordering within {111} planes. In these planes, spins in adjacent {111} planes align antiparallel to each other (see Figure 2) [39–41]. Below T_N, this AFM ordering causes magnetostriction, resulting in the formation of twinned crystal domains within the NiO crystal. This twinning produces four distinct magnetic twin domains (T domains), each characterized by different contractions along the {111} axes. Within each T domain, there are three possible spin easy axes oriented along the {112} directions, leading to a total of 12 different spin domains (S domains). This exchange striction leads to a small contraction of the distance between the ferromagnetically ordered planes below T_N. Despite this deviation from perfect cubic symmetry, the difference in plane spacing is only about 0.1% at 300 K.

Figure 2c depicts the overlap between the oxygen p-orbital and the nickel d-orbital. The fully occupied 2p orbital of oxygen, with its antiparallel electron configuration following the Pauli exclusion principle, induces opposite spin orientations in the nickel atoms' 3d electrons through a superexchange interaction. This type of exchange via a nonmagnetic ligand is a well-known phenomenon in metal oxides, first reported by Kramers for MnO [42,43].

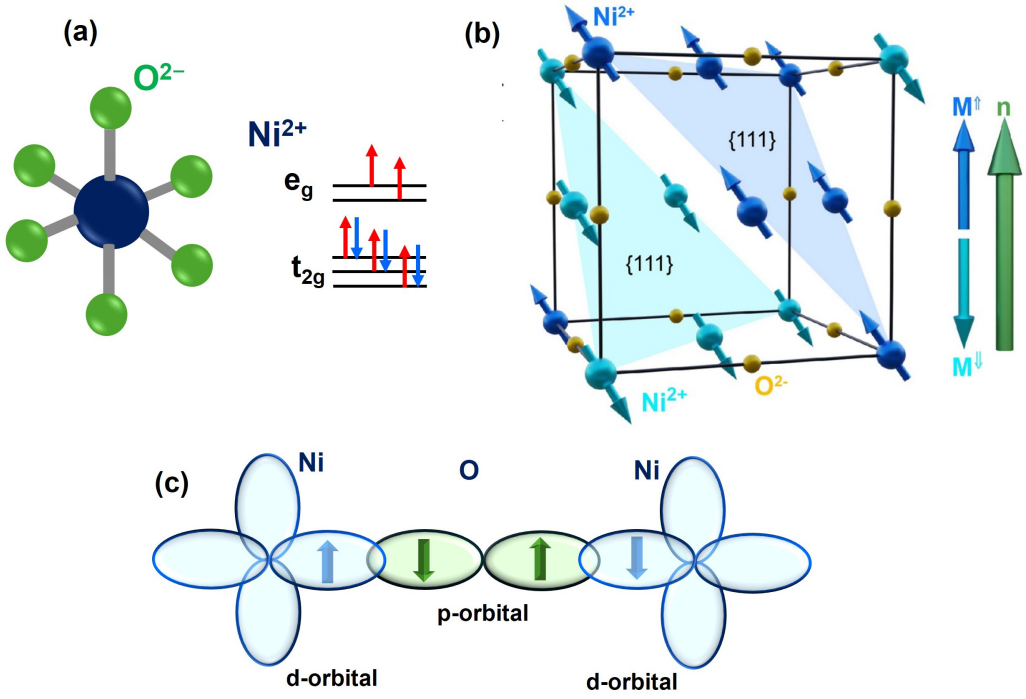

Figure 2. Panel (**a**) illustrates Ni^{2+} ions in octahedral coordination with O^{2-} ions, resulting in the splitting of d orbital electrons into t_{2g} and e_g sublevels. (**b**) The crystallographic and magnetic structure of NiO is displayed, showcasing the two Ni^{2+} sublattices ($M\uparrow$ *and* $M\downarrow$) and defining the Néel vectors as $n \equiv M\uparrow - M\downarrow$ [39]. (**c**) Schematic representation of the overlap between the p-orbitals of O atoms and the d-orbitals of Ni atoms. The combination of hopping-mediated AFM coupling and the singlet state of the fully occupied O orbitals results in a long-AFM ordering in NiO.

2.2. Magnetic and Structural Characterization Techniques

Understanding the inherent physical and chemical features of NiO NPs requires the application of several characterization techniques [44]. This section focuses on standard methods used to elucidate the main magnetic, structural, and compositional features of NiO NPs, while advanced techniques, although useful for single particle experiments, are not the primary focus of this review.

2.2.1. Magnetic Characterization of NiO NPs

They are dominated by pronounced surface effects arising from numerous uncompensated spins, which can also be present throughout the entire volume of the particle. Additionally, the odd number of sublattice planes and multiple sublattices due to finite-size effects can further contribute to the net magnetic moment observed [1,42]. These spins can exhibit superparamagnetic (SPM) behavior [45], for which thermal energy is sufficient to flip the magnetization within the particles spontaneously. Consequently, no magnetization is observed in the absence of a magnetic field. Interestingly, when a magnetic field is applied, there is a preferential orientation for the uncompensated spins, resulting in a net magnetic moment (see Figure 3). This alignment is analogous to that in a paramagnet but with higher magnetic moment, which can be up to 10^2 times larger than that of an atomic paramagnet [3]. Hysteresis loops (M–H) and zero-field cooled/field cooled (ZFC/FC)

curves are the most commonly used measurements to examine the influence of an external magnetic field on the magnetic response of NiO NPs (see Figure 3) [1,2,4,44].

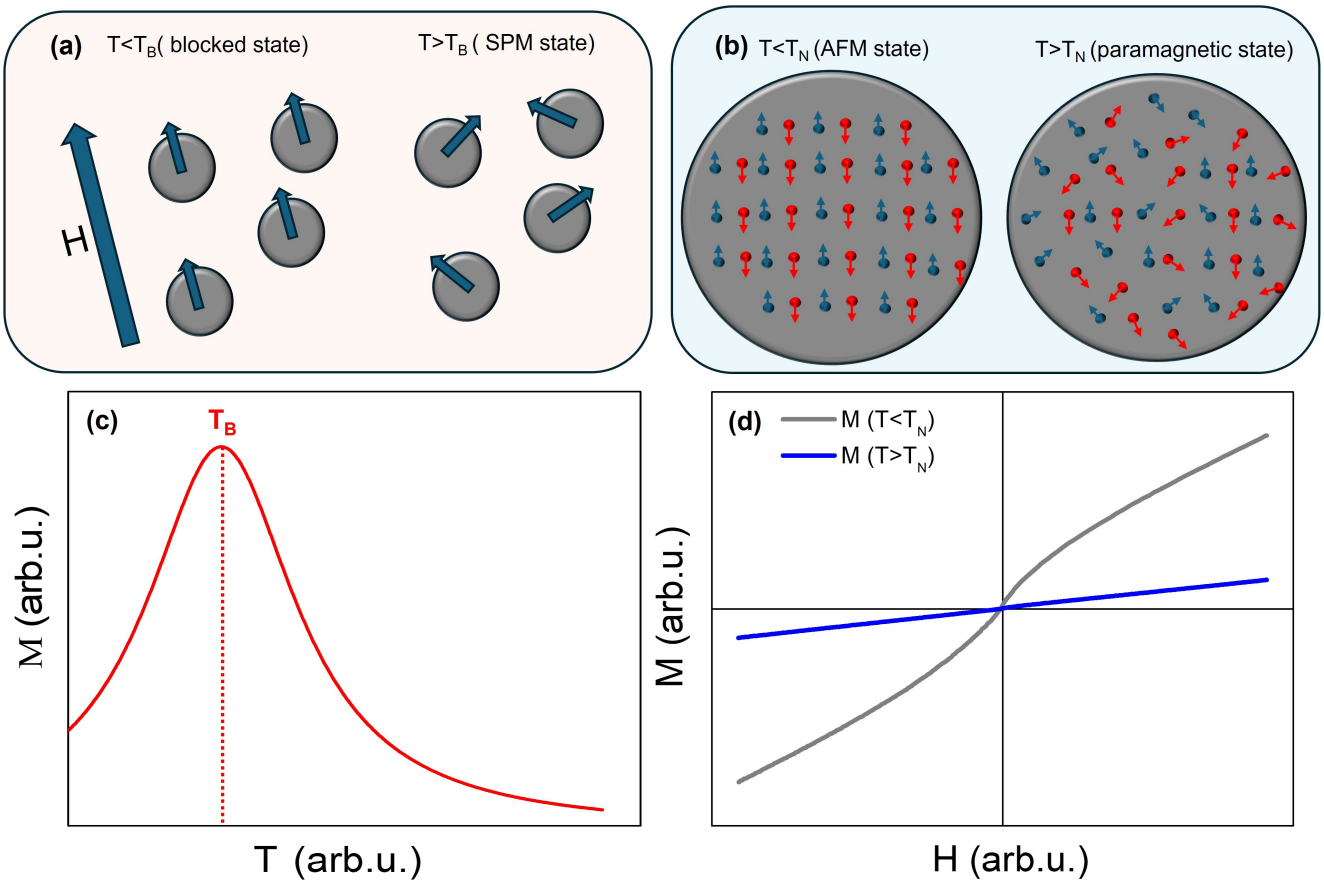

Figure 3. From left to right, the effect of temperature on the magnetic properties is shown: (**a**) Schematic representation of the magnetic states in NiO NPs under the influence of an external magnetic field below T_N. The left side of the panel shows a blocked state ($T < T_B$), while the right one shows a SPM state ($T > T_B$). (**b**) Effect of the temperature on the AFM order. The left side shows $T < T_N$, with a well-ordered antiparallel spin alignment in NiO NPs, and the right side depicts the paramagnetic state ($T > T_N$) with disordered spins, indicating the collapse of AFM order at higher temperatures. (**c**) M_{ZFC} curve highlighting T_B. (**d**) Hysteresis loops of NiO NPs below and above T_N are represented by grey and blue solid lines, respectively.

Measuring hysteresis loops at a constant temperature provides crucial insights into the magnetic properties of materials, specifically determining the maximum magnetization (M_{max}), zero-field saturation magnetization (M_s), remanent magnetization (M_r), and coercive field (H_c) [2,4]. The former is the highest net magnetization that a magnetic system can achieve by the action of a high enough external magnetic field. However, in AFM NiO and other AFM materials, full saturation is unreachable at any experimentally achievable magnetic field due to the intrinsic antiparallel alignment of magnetic moments and the effective large magnetic anisotropy. Therefore, the induced magnetization at any arbitrary value of the magnetic field is usually much smaller compared with that of a FM material. On the other hand, the weak FM behavior arising from either incomplete compensation between the two AFM sublattices or other more complex sublattice configurations within the NP due to finite-size effects can be measured by the so-called zero-field saturation

magnetization, M_s. In the high magnetic field region, hysteresis loops at low temperature in the blocked state are typically linear and can be fitted to

$$M(H) = M_s + \chi_d H \quad (1)$$

where χ_d is the high-field differential susceptibility that accounts for the uncompensated spins. M_s and χ_d are obtained from the average of the $H \rightarrow \pm H_{max}$ branches [2,4,46,47]. To recapitulate, M_{max} is used when the hysteresis loop is dominated by the AFM component, while M_s refers to the weak, superimposed FM component. Next, M_r is the value of the residual magnetization when the applied magnetic field is removed (H = 0). H_c corresponds to the magnetic field that must be applied to cancel the sample magnetization. It is determined by $H_c = \frac{(|H_c^+|+|H_c^-|)}{2}$, where H_c^+ and H_c^- are the intercepts of the hysteresis loop branches with the H-axis [2,4]. Interestingly, the interaction between FM and AFM phases can be evaluated by examining the shift in hysteresis loops, known as exchange bias phenomenon. This can be performed by recording hysteresis loops at low temperatures, after cooling the samples from room temperature to the desired low temperature under an applied magnetic field. The exchange bias field (H_{eb}) is then calculated as $H_{eb} = \left(H_c^+ - H_c^-\right)/2$ [2,4,46,47].

ZFC-FC curves are, on the other hand, commonly used for obtaining information about the distribution of magnetic volumes, verifying dipolar interactions, and estimating the average particle anisotropy in NP systems [4,48]. This protocol involves measuring particle magnetization as a function of temperature while subjecting the sample to a specific temperature/magnetic field profile. Typically, samples are cooled from room temperature to low temperatures (2–10 K) without an applied magnetic field. Then, a static magnetic field ($H > H_c$) is applied, and the zero-field-cooled (ZFC) magnetization (M_{ZFC}) is measured as the temperature increases [1]. Once room temperature is reached, the sample undergoes another cooling/heating cycle under the same magnetic field, and the field-cooled (FC) magnetization (M_{FC}) is collected during heating.

Initially, in a ZFC-FC protocol, as the sample is cooled in the absence of a magnetic field, the particle moments become blocked in random directions, resulting in very low magnetization. Then, as the sample is subsequently heated under the applied magnetic field, the particle moments progressively align with the external magnetic field, leading to a steady increase in net magnetization. This process continues until a peak is reached. Here most particles align with the magnetic field as they fluctuate between blocked and superparamagnetic states. Considering isolated SPM particles, we can define this temperature as the blocking temperature (T_B) [2,4,32], as follows:

$$T_B = \frac{K_{eff} V}{k_B \ln\left(\frac{\tau_m}{\tau_0}\right)} \quad (2)$$

where K_{eff} is the effective magnetic anisotropy constant, V is the volume of the NP, τ_m is a characteristic measuring time usually around 100 s, and $\tau_0 = 10^{-10}$ s is the characteristic relaxation time. On the contrary, M_{FC} curve, obtained by cooling and heating the sample in the presence of a magnetic field, shows no peak because, during cooling, the particle moments progressively align with the magnetic field, increasing M_{FC} as more particles become blocked. Upon heating, M_{FC} curve shows a gradual decrease in magnetization due to thermal excitation. Finally, T_N corresponds to the critical temperature at which the AFM order collapses. Below T_N, NiO NPs exhibit antiparallel spin alignments, characteristic of the AFM configuration. Above T_N, spins progressively disorder, as the remaining local AFM order vanishes, and paramagnetic behavior emerges.

2.2.2. Transmission Electron Microscopy (TEM)

This powerful technique allows a precise determination of NiO NPs' size and shape, which can range from a few to several tens of nm [49–51]. Direct visualization through TEM enables measurement of particle size distribution and provides insights into phenomena

like particle aggregation or sintering. Histograms of the size distributions of these systems can be determined by measuring some hundreds of particles using digital image analysis softwares and fitting the data commonly to a log-normal probability distribution [52], originating from the multiplicative processes involved in particle growth. The log-normal probability distribution can be described by Equation (3) [2,53,54].

$$P(D) = \frac{1}{S\sqrt{2\pi}D} e^{-\ln^2\left(\frac{D}{D_0}\right)/(2S^2)} \quad (3)$$

where D is the particle diameter, D_0 stands for the most probable value of D, and S is the standard deviation of the distribution of the logarithm of the reduced diameter D/D_0. D_0 and S are determined by fitting experimental histograms obtained from TEM data to Equation (3). The mean particle size D_{TEM} and the standard deviation σ of the diameter distribution are computed from Equations (4) and (5), respectively, as follows:

$$D_{TEM} = D_0 e^{S^2/2} \quad (4)$$

$$\sigma = D_0 e^{S^2/2}\sqrt{e^{S^2}-1} \quad (5)$$

Finally, the polydispersity index σ_{RSD} of the samples is estimated by dividing the standard deviation by the mean particle size $\sigma_{RSD} = \sigma/D_{TEM}$.

TEM also offers detailed observations of the surface roughness and porosity of NiO NPs. These surface characteristics are vital for applications that rely heavily on surface interactions, such as catalysis and sensors. Variations in surface texture, influenced by factors like synthesis methods and postsynthesis treatments, can affect the nanoparticles' optical, electronic, and catalytic properties [7–9].

High-resolution TEM (HRTEM) takes this analysis a step further, enabling a highly detailed examination of NiO NPs' crystallinity. HRTEM achieves this by directly imaging crystal planes and measuring the spacings between them. HRTEM also plays a crucial role in identifying defects within the crystal structure, such as dislocations or stacking faults, which have a significant impact on the physical and chemical properties of the NiO NPs, often influencing factors like electronic properties and catalytic activity. Additionally, structural and compositional analyses through techniques integrated with TEM, such as Selected Area Electron Diffraction (SAED) or Electron Energy Loss Spectroscopy (EELS), can confirm the chemical purity of NiO NPs [49–51].

SAED patterns of typical NiO NPs show ring-like patterns, indicating the random orientation of many small crystals. Analysis of these patterns is in general straightforward, as pure NiO presents a high-symmetry FCC crystal structure, so fewer rings are visible because many lattice planes are equivalent [38].

Analysis of EELS spectra helps detect both the presence of any additional phases and assess the structural crystallinity, which is essential for applications requiring consistent and reliable performance from the particles [55]. This technique is based on inelastic scattering phenomena, such as band transitions and phonon or plasmon excitations, and requires a more complex data processing and spectrum understanding. The area of interest for NiO comprises the O K-edge at (530–545 eV) and the Ni L-edges (853 eV L_3, 870 eV L_2), which form the so-called 'core-loss spectrum', where signals originate from excitations of inner-shell electrons to the conduction band; hence, the intensity of the signal can be directly related to the proportion between elements.

2.2.3. Scanning Electron Microscopy (SEM)

Similarly to TEM, SEM allows the study of NiO NP size, topography, and surface composition, trading resolution for cost-effective and simpler operating procedures [56]. SEM can complement TEM by better visualizing larger particles or agglomerated samples, where electron transparency is compromised, especially in metal oxides with particles larger than 30 nm. In addition to size and topographic information, SEM can provide

compositional mappings using backscattered electrons. Many SEM systems include Energy-dispersive X-ray (EDX) add-ons, which analyze X-ray radiation emitted when sample electrons return to relaxed states. Depending on the synthesis method, a typical NiO spectrum contains O Kα and Ni Kα/Lα signals, along with traces of other elements like carbon. EDX can detect contamination and estimate the nickel-to-oxygen ratio. Area mappings can reveal compositional differences between the bulk and the surface of NPs, which is useful for identifying core–shell systems and detecting Ni/NiO coexistence.

2.2.4. X-ray Diffraction (XRD)

XRD plays a pivotal role in confirming the phase purity and crystallinity of NiO NPs [57]. XRD patterns provide a wealth of information, including the lattice parameters and symmetry of the crystal structure. This allows for the identification of the crystal structure [7–9]. Figure 4 shows the typical Bragg diffraction peaks observed in an XRD spectrum of these systems, which correspond to specific planes within the crystal lattice. This XRD spectrum typically exhibits peaks at 2θ values of 37.2°, 43.3°, 62.9°, 75.4°, and 79.4°. These correspond to the (111), (200), (220), (311), and (222) crystal planes of NiO, respectively. It is worth mentioning that the variation in intensities of these peaks could suggest a preferential growth along other crystal planes, while the presence of unexpected peaks could indicate potential impurities in the NiO NPs, such as metallic Ni or nickel (III) oxide (Ni_2O_3).

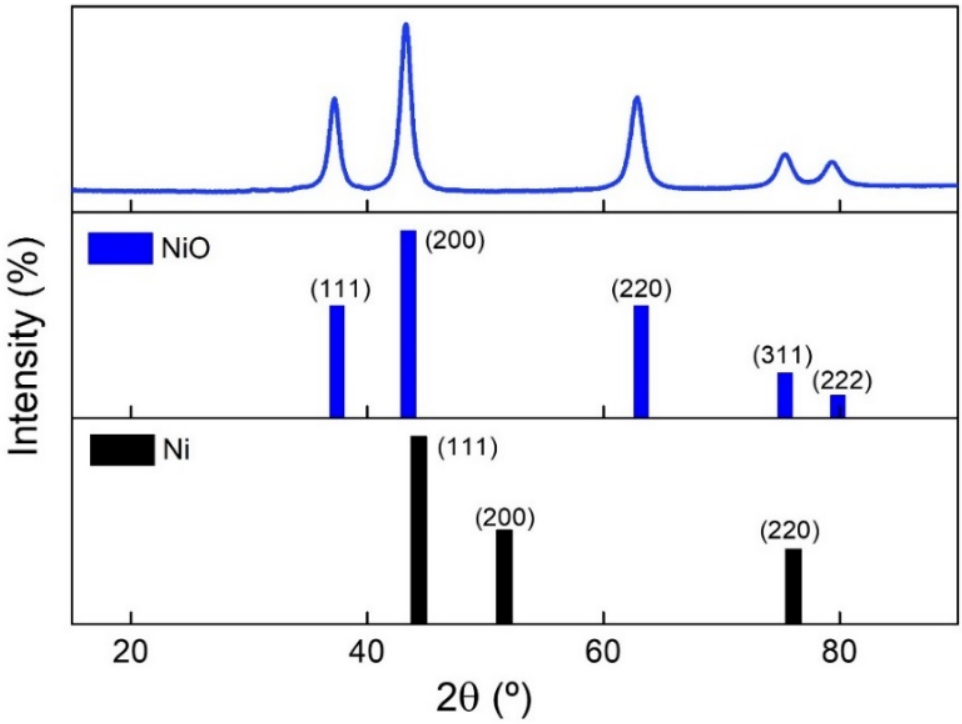

Figure 4. XRD characterization of NiO NPs. The upper panel displays a typical XRD spectrum of NiO NPs, with intensity plotted against the diffraction angle (2θ) ranging from 15° to 90°. The lower panel presents the Bragg diffraction peaks for both NiO and Ni phases, highlighting their respective characteristic peaks [7–9].

Accurate determination of these planes and their properties requires comparing the experimental XRD pattern with standard or computed patterns for NiO. The Scherrer–Debye Equation shown in Equation (6) is often used to estimate crystal size (D) [58].

$$D = \frac{K\lambda}{\beta \cos\theta} \quad (6)$$

where K is a dimensionless shape factor, λ is the X-ray wavelength, β is the line broadening at half the maximum intensity (FWHM), and θ is the Bragg angle. This equation helps estimate the size of crystallites in a material based on the broadening of XRD peaks, assuming that the broadening is due to small crystal size rather than strain or other factors.

Beyond structure identification, XRD offers valuable insights into the size of NiO NPs. By analyzing the broadening of diffraction peaks, techniques like Scherrer's formula can be used to estimate the size of the crystallites. This information is crucial for understanding the catalytic and electronic properties of the NPs. Smaller particles generally possess a higher surface-area-to-volume ratio, which enhances their reactivity.

XRD can also detect strain within the crystal lattice, which can arise from distortions or defects. This strain can significantly impact the electronic properties and stability of the NPs. The technique's ability to detect both microstrain and macrostrain provides a comprehensive picture of the internal stresses affecting the crystalline structure.

For a more detailed picture, XRD can be used in conjunction with other techniques like Rietveld refinement [59]. This process helps extract quantitative data on the crystal structure, such as the atomic positions and occupancy within the lattice. This information is essential for tailoring the properties of NiO NPs for specific applications. Rietveld refinement essentially achieves a more accurate fit between the observed and calculated diffraction patterns, leading to a deeper understanding of the structural parameters.

2.2.5. X-ray Photoelectron Spectroscopy (XPS)

XPS is a key analytical tool for evaluating the surface chemistry and electronic properties of NiO NPs [60]. It provides insights into the elemental composition, empirical formulas, and oxidation states by analyzing the kinetic energy and number of electrons emitted from the material's surface after X-ray irradiation. In particular, XPS is crucial for understanding the electronic structure of Ni 2p core electrons in NiO NPs (see Figure 5) [61,62]. These Ni 2p orbitals, which are degenerated into two components, $2p_{3/2}$ and $2p_{1/2}$, due to spin-orbit coupling with relative intensities 2:1, are of great interest in XPS, as 2p orbitals of transition metals have high photoionization cross-section, yielding relatively high values of the electron ejection probability, and, hence, resulting in well-defined and intense peaks. Another advantage is that the binding energy of 2p orbitals is highly dependent on interactions with oxygen that can be attributed to the oxidation state of Ni. The main Ni $2p_{3/2}$ peak, typically at about 854 eV, indicates nickel in the +2-oxidation state, characteristic of Ni(II) in the NiO lattice. It is often accompanied by a second $2p_{3/2}$ component related to interactions with nonlocal oxygens, surface effects, and the presence of Ni^{3+}. The Ni $2p_{1/2}$ peak appears around 872 eV due to the spin-orbit splitting of the Ni 2p electrons. Satellite peaks, observed around 862 eV for Ni $2p_{3/2}$ and approximately 879 eV for Ni $2p_{1/2}$, arise from interactions between the photoelectron and unpaired electrons in the valence band, which are indicative of the material's correlated electronic nature. The oxygen 1s peak in NiO, centered around 529.5 eV, signifies oxygen ions in the oxidized form and provides data on the oxygen environment. Shifts in this peak position can indicate variations in the electronic environment, potentially due to oxygen vacancies or interactions with other elements. Quantitative information is usually taken from consulting the signal ratio between Ni and O, since from the Ni 2p peaks analysis one can quantitatively differentiate Ni^{2+} from metallic nickel, yet it is not as straightforward with Ni^{3+}. Note that in some cases the surface of the particles can present oxygen excess from the atmosphere, hence, it is recommended to perform Ar^{+} sputtering using the lowest possible ion beam energy to minimize reduction effects.

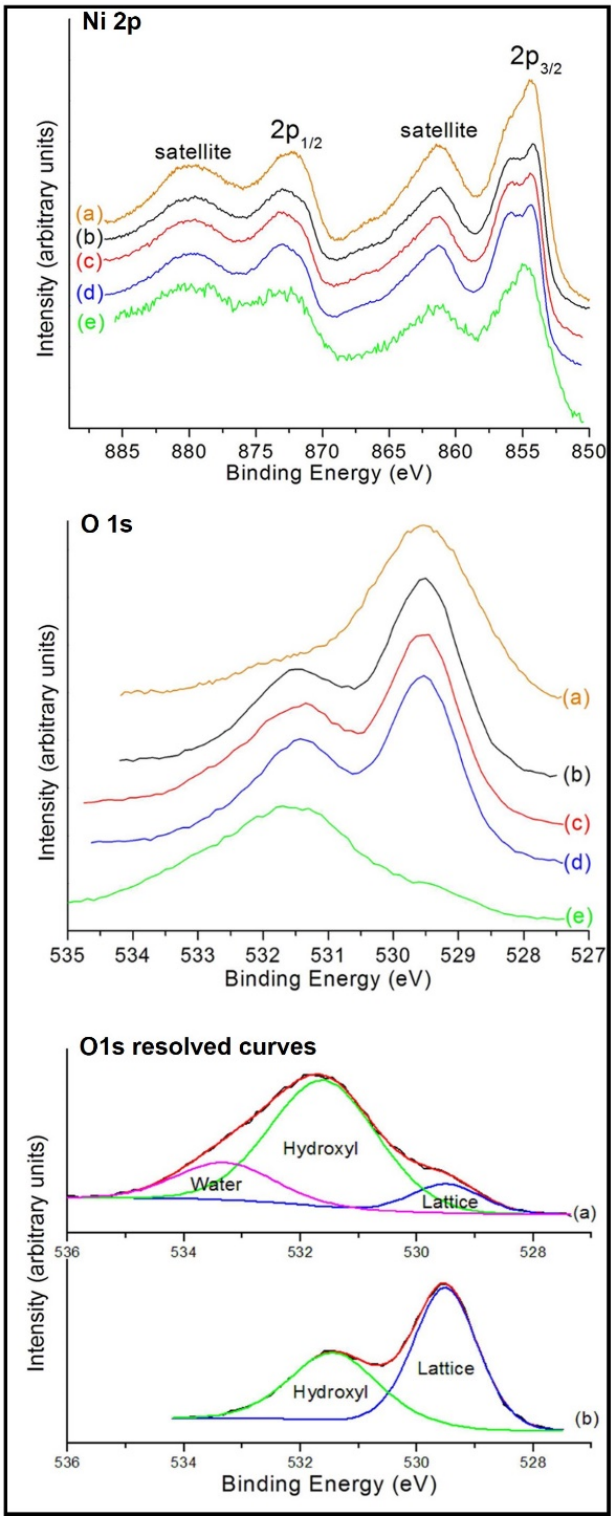

Figure 5. Comparison of the XPS spectra for different sizes of NiO NPs [61]: (a) Bulk NiO, (b) 25 nm NiO NPs, (c) 10 nm NiO NPs, (d) 5 nm NiO NPs, and (e) Hydroxylated NiO NPs. The upper panel shows the Ni 2p XPS spectra, displaying the binding energy peaks for Ni $2p_{3/2}$ and Ni $2p_{1/2}$, along with satellite features. The middle panel presents the O 1s XPS spectra, containing binding energy peaks corresponding to lattice oxygen and surface hydroxyl groups. The lower panel shows the resolved O 1s curves, highlighting the contributions from lattice oxygen, surface hydroxyl groups, and adsorbed water for bulk NiO and 25 nm NiO NPs. The spectra illustrate the distinct contributions of lattice oxygen and surface hydroxyl groups, particularly for the 25 nm NiO NPs.

3. Chemical Approaches to Synthesized NiO NPs

A wide range of synthetic pathways has been developed to synthesize NiO NPs, allowing precise control over various aspects such as particle size, structural shape, crystallinity, and magnetic properties [7–9]. Two predominant approaches are commonly used for NiO NP preparation: the top-down and bottom-up methods. The former uses macroscopic initial structures, whose size is reduced in the nanoscale range by physical methods, such as, among others, laser ablation [63,64], mechanical milling [65], nanolithography [66], and sonochemical methods [67]. The major disadvantages of this approach are the high cost and notable difficulty in controlling the size of NPs, which specifically for NiO is a critical parameter as particles tend to agglomerate at larger sizes and adopt irregular pseudo-spherical shapes. On the other hand, bottom-up approaches focusing mainly on chemical and biological routes have become increasingly popular. This preference stems from several advantages, including reduced production costs, enhanced reaction yields, and superior control over the spatial characteristics of the resulting system. Nevertheless, a significant limitation is the need for annealing to convert the particles into their oxidized form. Given the predominant use of chemical routes in NiO NP synthesis for fundamental studies, this review is focused on these methods, detailing the main characteristics of the routes (see Table 2). Additionally, Figure 6 summarizes some typical morphologies synthesized through diverse chemical routes.

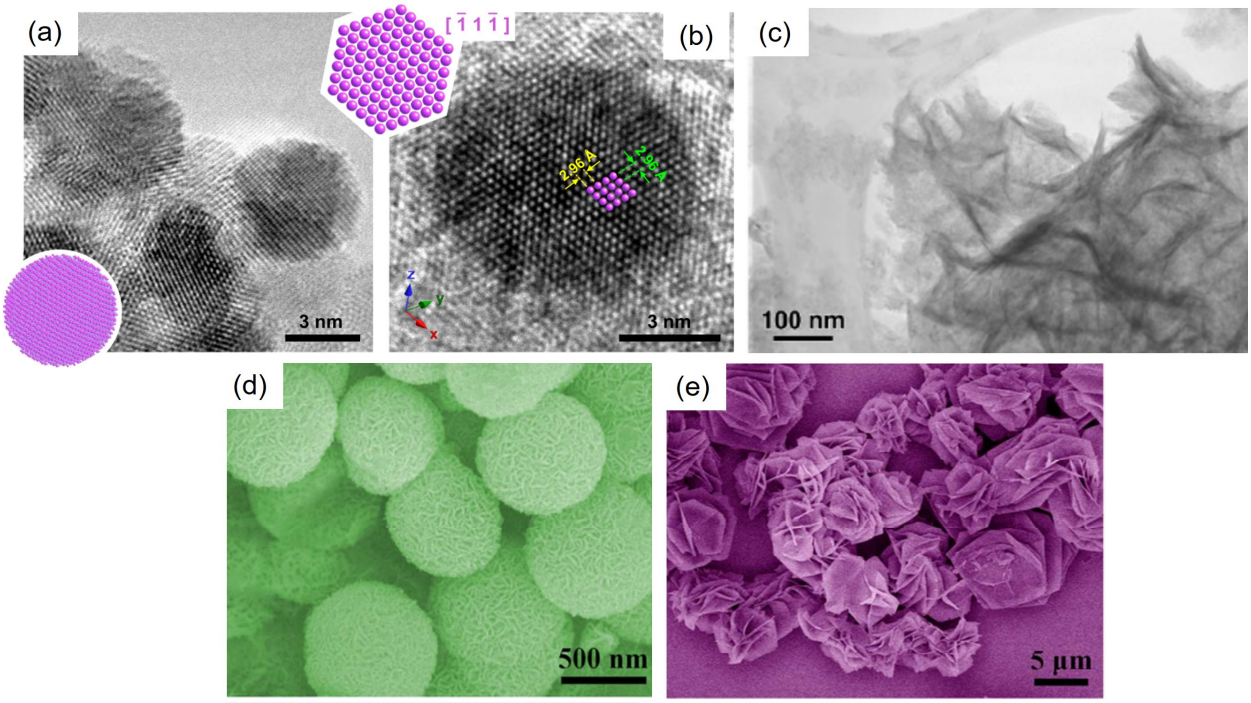

Figure 6. Distinct morphologies obtained from NiO NPs: (**a**) TEM image showing spherical NiO NPs with high crystallinity [68]. (**b**) HRTEM image illustrating the atomic arrangement and lattice fringes of NiO NPs [68]. (**c**) TEM image depicting rod-like NiO NPs [69]. (**d**) SEM image showing silk-flower NiO NPs [70]. (**e**) SEM image showing flower-like NiO nanostructures [71].

Table 2. Main chemical approaches for synthesizing NiO NPs detailing their pros and cons.

Synthesis Method	NP Range of Sizes (nm)	Morphologies	Pros	Cons
Co-precipitation [31,72,73]	~10–100 nm	spheres, cubes	Straightforward, low-cost, easy to scale up	Poor control over crystal quality and morphology compared with other methodologies
Hydrothermal [12,17,29,35,74]	~10 nm up to microns	spheres, rods, plates, flowers	Decent control over composition, relatively simple experimental setups	Lower crystallinity unless posterior annealing, need for specific instrumentation, lengthy reaction times, and difficulty in monitoring reaction
Sol-gel [32–34,39]	~10–100 nm	spheres, cubes, rods	Simple, cost-efficient process, high reaction yields, and scalability	Limited control over particle morphology, often involves a last-step calcination
Thermal decomposition [36,37,75–79]	~5–50 nm	spheres, cubes, hexagons, branches	Precise control over size, morphology, crystallinity, and composition	Requires many reagents, challenging to scale up and to reproduce
Microwave Assisted [25,28,80,81]	~5–50 nm	spheres, cubes	Rapid synthesis, high reaction yields, and scalability	High initial setup cost, limited size control

3.1. The Coprecipitation Method

In the realm of chemical bottom-up synthesis methodologies, coprecipitation stands out as one of the most utilized approaches for the obtention of NiO NPs. This technique is based on dissolving one or more soluble metal salts in aqueous media, followed by their precipitation induced by a basic pH [73]. The precipitated compounds, which typically form insoluble metal hydroxides or carbonates, require subsequent annealing to convert them into the NiO phase. Most common nickel salts employed include nickel(II) chloride hexahydrate ($NiCl_2 \cdot 6H_2O$) or nickel(II) nitrate hexahydrate ($Ni(NO_3)_2 \cdot 6H_2O$) compounds. The precipitation is generally induced utilizing hydroxide or carbonate salts, such as sodium hydroxide (NaOH), ammonium hydroxide (NH_4OH), or hydrogen sodium carbonate ($NaHCO_3$).

The main strength of this route lies in its rapid and simple steps, as well as the low cost of the reagents and experimental setup required. These advantages make the coprecipitation method one of the most scalable chemical synthesis techniques available. However, the simplicity of the process is accompanied by low control over the crystal quality and morphology of the NPs. Consequently, a final annealing step is almost invariably required to improve the quality of the NiO NPs.

To illustrate the applicability of these systems, recent examples of NiO NPs are described in detail as follows. Rahal et al. presented a synthetic route to make 30 nm NIO NPs based on the capping of nickel(II) chloride with EDTA [72], followed by the dropwise addition of 4 M NaOH to adjust the pH to 12, inducing the precipitation of a green product. This product was then washed and air dried at 90 °C for 24 h. The dried powder was heated at 500 °C for 5 h to obtain black NiO NPs. The resulting particles were spherical, with sizes around 30 nm, displaying weak agglomeration but high polydispersity. Hysteresis loops at room temperature show typical trends of AFM NPs such as low H_c, M_r, and magnetization values probably due to the large crystal size of the particles.

The presence of metallic nickel is sometimes a significant issue that researchers must deal with. Factors such as type and amount of surfactant, annealing temperature and times are key aspects to control the Ni (II) reduction process. Sabouri et al. reported an interesting work focused on developing a green chemistry pathway for investigating the cytotoxicity of NiO NPs on cancerous cells [82]. The chosen nickel precursor and precipitation agent

were $Ni(NO_3)_2 \cdot 6H_2O$ and NH_4OH, respectively, in a molar ratio of 1:4. The study's main innovation was the addition of soluble starch to the mixture, which could stabilize the formation of small particles. Following a 1 h reaction at 60 °C and subsequent drying at 100 °C for 12 h, nickel hydroxide ($Ni(OH)_2$) particles were obtained. Calcination of these particles at 300–600 °C for 2 h yielded spherical NiO NPs with diameters below 40 nm. Magnetic measurements, specifically hysteresis loops, revealed a superimposed FM behavior with M_s of approximately 15 emu/g, likely due to the presence of metallic nickel, as was corroborated by XRD spectra.

NiO NPs can also serve as templates for the addition of other metals to enhance or modify their magnetic properties. Gandhi et al. illustrated the magnetic properties and applications of NiO and Fe-doped NiO nanocomposites for magnetic memory effects [29]. In their study, $Ni(NO_3)_2 \cdot 6H_2O$ and $Fe(NO_3)_3$ were mixed in deionized water, followed by the addition of ammonium bicarbonate (NH_4HCO_3) to promote coprecipitation. The resulting light green precipitate was dried at 100 °C for 12 h and then annealed at 600 °C for 4 h in a muffle furnace. Magnetic studies revealed that Fe-doping enhances intraparticle interactions and gives rise to additional magnetic anisotropy barriers. For the undoped NiO NPs, they were found to be spherical with an average diameter of 63 nm, exhibiting complete AFM behavior, as expected for particles in this range of sizes.

3.2. Hydrothermal Synthesis of NiO NPs

The hydrothermal method is a chemical synthesis process involving two main stages. Initially, a metal hydroxide is formed by dissolving a selected metal precursor in water [83]. Subsequently, this hydroxide undergoes dehydration under medium to high pressures in autoclaves, leading to the formation of the NiO phase (see Figure 7). This method is particularly dependent on the solubility of the metal precursor in water, in addition to requiring high temperatures and pressures. A significant advantage of hydrothermal synthesis is its ability to produce crystalline phases that would be unstable under normal conditions. However, the method does not consistently produce materials with high crystallinity; some studies have reported the formation of amorphous precipitates. To address this, an annealing process is often employed post synthesis to enhance the crystallinity of the final product. This additional step involves heating the material at controlled temperatures to improve its structural properties.

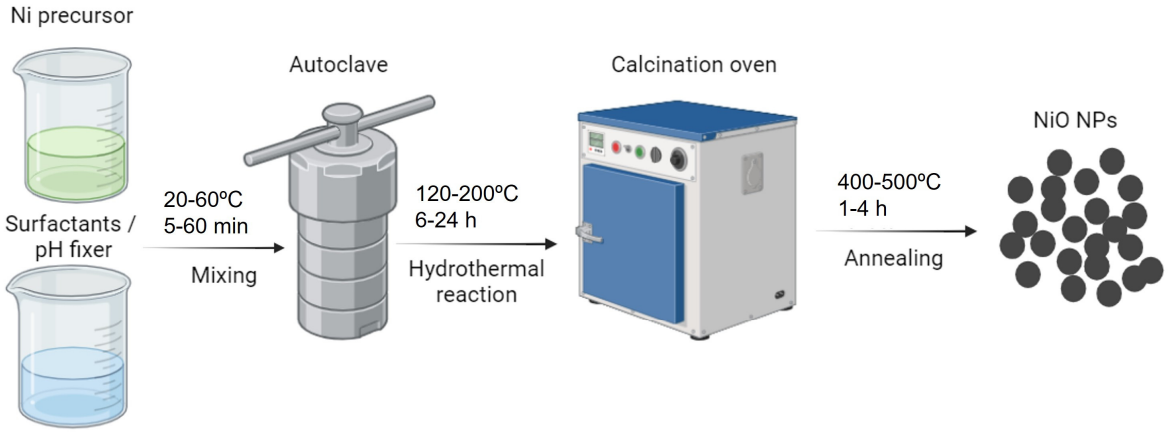

Figure 7. Schematic illustration of a typical hydrothermal synthesis process for NiO NPs (Figure created with BioRender.com). The synthesis process starts by mixing the Ni precursor with surfactants at low temperatures until full dissolution. Then, the reaction mixture undergoes a hydrothermal reaction in an autoclave at high temperatures for times ranging from 6 to 24 h. The resulting product may then be subjected to calcination in an oven at high temperatures for times ranging from 1 to 4 h leading to the formation of NiO NPs.

Liu et al. reported the synthesis of two distinct flowerlike NiO structures combining a facial hydrothermal method coupled with subsequent annealing [71]. Their precursor of choice was $Ni(NO_3)_2 \cdot 6H_2O$, which they dissolved in an aqueous solution in conjunction with mixtures of either ammonium fluoride (NH_4F) and urea to form 'rose' flowers or sodium acetate (NaAc) and ethylene glycol to obtain 'silk' flowers (see Figure 8). The hydrothermal reactions were conducted for 6 h in a Teflon-lined reactor with temperatures ranging from 120 °C to 180 °C based on the specific flower morphology. Finally, both structures were annealed at 350 °C for 2 h. The petal nanosheets had an average diameter of 0.7–1.0 µm for silk-flower architectures and 4–7 µm for rose-like, with a thickness of 11 nm and 25 nm, respectively. Magnetization was measured for both structures and found analogously to exhibit SPM loops with M_s in the range of 8–10 emu/g. The authors attribute these values to synergistic effects of broken bonds and lattice distortion, which could be plausible as no metallic Ni traces were detected based on their obtained XRD patterns.

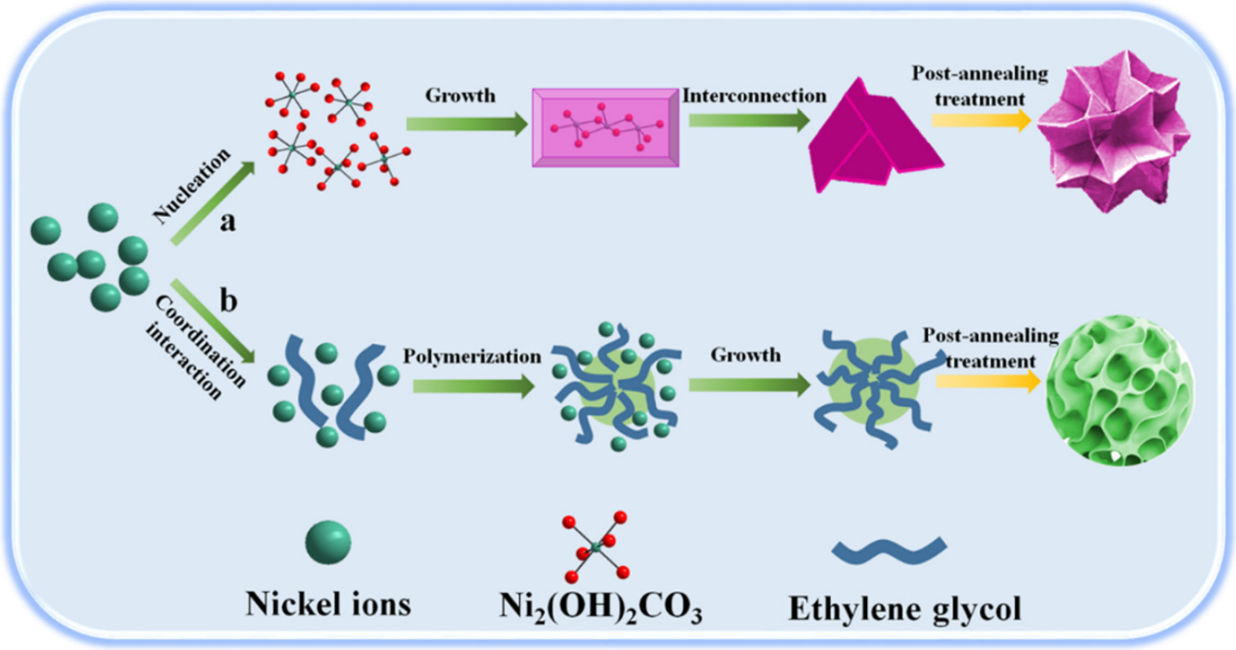

Figure 8. Proposed reaction mechanisms for the formation of (a) rose-flower NiO and (b) silk-flower NiO by a hydrothermal route [71].

In addition to the traditional hydrothermal synthesis using an autoclave, more advanced systems can be employed. Cooper et al. conducted a study on core/shell magnetism in NiO NPs [35]. The hydrothermal synthesis was performed inside a confined jet mixer by reacting a supercritical water flow (450 °C, 24.1 MPa) with a second flow of 0.08 M $Ni(NO_3)_2$ and a third flow of 0.1 M KOH solution, both at 175 mL/min. The primary advantage of using this sophisticated experimental setup is the elimination of the final annealing step while maintaining precise control over system conditions. The resulting particles were spherical with a core/shell structure, featuring an AFM 5.2 nm core and a disordered 0.7 nm shell. The hysteresis loop exhibited a characteristic 'S' pattern, which did not reach saturation even at $H > 60$ kOe probably due to the strong AFM-FM interactions in the core@shell NP structure.

In a more recent study, Zenkin et al. described the green hydrothermal synthesis of NiO and NiO@ZnO NPs for supercapacitor applications [74]. An amount of 7 mmol of $Ni(NO_3)_2 \cdot 6H_2O$ was dissolved in water and combined with 25 mL of *S. officinalis* plant extract, which is a natural reducing and capping agent used in traditional medicine. To regulate the pH, 0.1 M NaOH was added to the solution, and the final mixture was transferred to a 100 mL autoclave and left to react for 24 h at 180 °C. A final annealing

at 500 °C for 2 h was then performed to obtain the NiO NPs. The achieved NiO NPs presented a spherical shape with an average size of 16 nm. Aggregation phenomena could though be observed as polydispersity was slightly above the expected (PI ≈ 25%). Hysteresis loops depicted a weak FM behavior for pure NiO NPs that was further reduced when integrated into a NiO@ZnO nanocomposite, foreseeable considering the diamagnetic ZnO contribution.

3.3. Thermal Decomposition

The synthesis of NiO NPs through this method involves the high-temperature decomposition of a nickel precursor with either organic solvents characterized by high boiling points or in solid media (see Figure 9) [4]. This multistep process requires higher temperatures, with reaction parameters playing a pivotal role in determining the outcome. By judiciously selecting the adjusting reaction time, controlling temperature, and choosing the appropriate organometallic precursor, researchers fine-tune NiO NP structural characteristics. Nickel oxalates, with their low melting points, are preferred precursors, yielding NPs with high surface area and small crystalline sizes. This method is often paired with TGA, granting a deeper understanding of the precursor's decomposition profile to finely tune the reaction conditions.

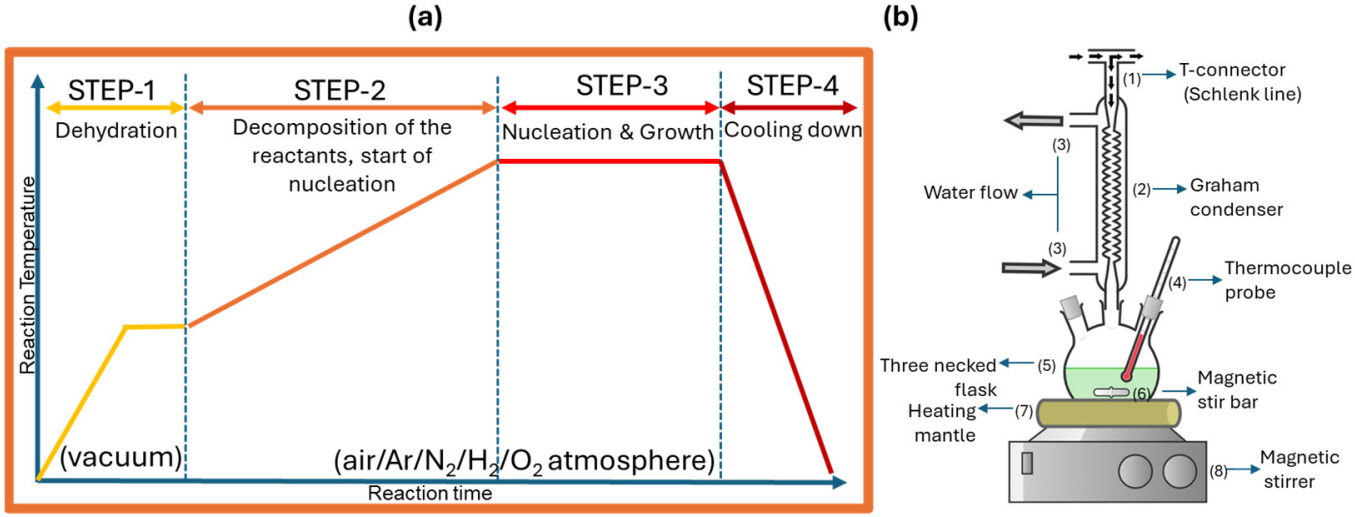

Figure 9. (**a**) Representation of the typical stages found in the thermal decomposition of Ni precursors in organic media (Figure created with Chemix). (**b**) A schematic representation of the experimental set-up detailing each part is shown.

Sharma et al. reported the synthesis of 6 nm NiO NPs via the thermal decomposition of nickel phosphine complexes in a high-boiling-point organic solvent [36]. The synthesis involved heating nickel phosphine complexes to 200 °C in the presence of trioctylphosphine oxide (TOPO) as a capping agent, resulting in the formation of NiO NPs with an average particle size of approximately 6 nm. These particles featured a crystalline core and a broad disordered surface shell, which accounted for about 75 ± 20% of the total particle diameter. Their findings indicated that magnetic behavior was primarily influenced by strong surface effects, especially at low temperatures.

Farhadi and Roostaei-Zaniyani demonstrated a low-temperature method for synthesizing NiO NPs, addressing the high energy consumption typically associated with such processes [75]. They prepared a Ni complex by combining $Ni(NO_3)_2 \cdot 6H_2O$ with excess ethylenediamine, precipitating the mixture with alcohol. The solidified crystals were then decomposed at temperatures between 200 and 400 °C for 60 min. The resulting spherical particles had an average size of 15.5 nm, although metallic nickel traces were found in samples annealed below 350 °C. Hysteresis loops of the NiO NPs prepared at 400 °C showed SPM behavior with a magnetization around 1 emu/g at 2 kOe.

Another interesting example was shown by Ibrahim et al. [76], who synthesized larger NiO NPs for fundamental studies using a Ni–Schiff base complex, followed by calcination. This Schiff base was prepared by condensing 2-hydroxy-1-naphthaldehyde (5 mmol, 0.86 g) with 2-aminopyridine (5 mmol, 0.47 g) in ethanol, refluxed for 1 h at 70 °C and purified. The Ni–Schiff complex was formed by reacting the Schiff base with a nickel nitrate precursor in ethanol at room temperature, followed by precipitation and heating to 500 °C in air for 1.5 h. This produced particles with an average diameter of 62 nm and noticeable polydispersity. Magnetic measurements indicated less significant SPM behavior compared with the 15.5 nm NPs, underscoring the size dependence of NiO magnetic properties. The hysteresis loop was measured up to 10 kOe, leaving the saturation behavior at higher fields undetermined.

An interesting advantage of thermal decomposition is its ability to be integrated as a final step in other synthetic pathways [84]. Gandhi and Lin studied H_{eb} in Ni/NiO NPs using a two-step process involving initial precipitation followed by thermal decomposition. $Ni(NO_3)_2 \cdot 6H_2O$ was mixed with oxalic acid in deionized water, with the acid added dropwise to promote precipitate formation, which was then washed to remove reactants and byproducts [85]. The precursor was heated to 300 °C for 1 h under an Ar atmosphere to obtain the metallic Ni phase, followed by a second air annealing at 300 °C to form the NiO shell. The resulting core/shell particles had a Ni core of 30 nm and a NiO shell ranging from 8.6 to 13.6 nm. Magnetic measurements confirmed the exchange coupling in the Ni/NiO structures, showing consistent magnetization curves regardless of shell thickness.

3.4. Sol–Gel Synthesis Route

This process represents a bottom-up chemical synthesis approach, wherein the hydrolysis and subsequent condensation of a precursor material led to the formation of a colloidal solution, followed by its posterior gelation to obtain a gel (see Figure 10) [86]. To enhance the properties of the synthesized material, an annealing step is employed, facilitating particle size growth, byproduct removal, and the conversion of reaction intermediates into the desired final product. The incorporation of a surfactant is critical within this process, as it regulates the growth of NPs and prevents excessive agglomeration. This method's versatility is underscored by its compatibility with both organic and inorganic nickel precursors, expanding its application range to a point where it is widely considered the most common method for NiO NPs synthesis. The sol–gel process is distinguished by its simplicity, involving straightforward setup requirements and the cost-effective nature of reactants and equipment. Despite this simplicity, it offers exceptional control over the particle size, morphology, and composition of the synthesized material. Thus, the ability to finely tune synthesis parameters without performing significant modifications to the synthetic route provides precise control over the final product unmatched by other alternatives.

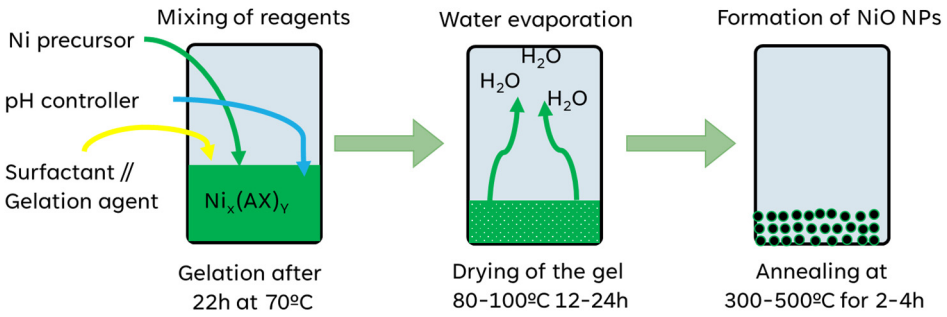

Figure 10. Sketch showing three typical steps to obtain NiO NPs. The process begins with the dissolution of nickel salts in a solvent, followed by the addition of a precipitating agent to form an insoluble metal hydroxide or carbonate (precipitate). This mixture is then subjected to a drying process. Finally, the dried precipitate undergoes calcination, resulting in the formation of NiO NPs.

Adiba et al. accomplished the synthesis of green NiO NPs by what is known as the citrate sol–gel method by mixing a solution of 0.01 mol of $Ni(NO_3)_2 \cdot 6H_2O$ with a 0.02 mol solution of citric acid [39]. The temperature was kept constant at 80 °C to perform the aging of the gel, following an annealing at 800 °C for 8 h. The obtained particles showed typical S-loops with small values of M_s and H_c , probably due to surface effects.

More exhaustive research was conducted by Jafari et al., who not only studied the magnetic properties of NiO NPs but also the effect of the annealing temperature and ambient as well [34]. In their investigations, they selected a sol–gel approach, $Ni(NO_3)_2 \cdot 6H_2O$ being the precursor of choice and gelatin type B the surfactant, both acting as protection and gelation agent. The gel was formed by dilution of both components in an aqueous medium at 80 °C for 12 h. No dedicated aging step was performed, since the green gel was directly annealed inside a crucible. The authors controlled both the furnace atmosphere (air and O_2) and the annealing temperature (400–800 °C), no concise heating duration was provided in the article. The particles obtained presented a spherical shape with average diameters ranging from 8 to 76 nm, proportional to the increase in calcination temperature. The hysteresis loops followed similar trends to what is expected for finite-size and surface effects, as samples with $D > 30$ nm present typical AFM behavior, while those under 15 nm show slight superparamagnetism. The latter is further highlighted in the case of NPs annealed under air atmosphere in comparison with O_2. A plausible explanation for these findings could be a minimal reduction of surface Ni^{2+} to metallic nickel when in the presence of atmospheric H_2.

3.5. Outlook on the Main Chemical Routes for Synthesizing NiO NPs

The synthesis approaches discussed above encompass the majority of the most common bottom-up chemical methods. They are briefly presented and described to provide a general overview of the advantages and drawbacks each method offers, which is crucial for selecting the most appropriate route based on specific needs.

For instance, coprecipitation is one of the most researched methodologies for the synthesis of NiO NPs and their integration into various applications, but it may not be the most suitable for fundamental studies. Similarly, hydrothermal synthesis is not ideally suited for magnetic studies because of the suboptimal crystallinity of the products. However, it is highly valuable for studies focused on obtaining exotic morphologies or phases.

Thermal decomposition and sol–gel methods are probably the most suitable for magnetic studies, especially the latter. The sol–gel method combines excellent control over the products by finely tuning the reaction parameters with cost-effectiveness. It can be seen as a more complex version of coprecipitation that trades simplicity for quality, with the gel acting as a template for particle growth, minimizing aggregation phenomena. Thermal decomposition, although not the simplest method, can be integrated as a final step for other synthetic techniques, making it quite versatile.

Other novel techniques, such as sono-chemical, microwave-assisted, pyrolysis, and nanocasting, are still in experimental stages. However, they have the potential to surpass existing mainstream methodologies shortly, as the synthesis of highly pure NiO particles remains a significant challenge. Another interesting methodology is the microemulsion method, which offers both advantages and drawbacks [87–89]. This technique involves creating a thermodynamically stable mixture of water droplets dispersed in an oil phase, stabilized by surfactants. Key steps include mixing an oil phase (e.g., cyclohexane), a surfactant (e.g., Triton X-100), and a cosurfactant (e.g., n-hexanol), followed by adding aqueous solutions containing the metal precursor and a precipitating agent. The resulting nanometer-sized droplets serve as reaction sites, allowing for precise control over particle size and morphology by adjusting the water-to-surfactant ratio and calcination temperature. While the microemulsion method provides excellent control over nanoparticle properties and requires simple apparatus, it also necessitates high annealing temperatures and is primarily limited to laboratory-scale synthesis, posing challenges for large-scale production.

Despite these hurdles, researchers continue to explore its potential in nanotechnology and materials science.

The essential parameters that must be precisely regulated during the synthesis of NiO NPs to ensure uniform size and morphology depend on the synthesis method employed. In the coprecipitation method, the concentration of the reactants, the pH of the solution, the temperature at which the reaction is carried out, and the rate of addition of the precipitating agent are key parameters. Variations in these parameters can affect the nucleation and growth processes, resulting in differences in particle size, distribution, and morphology. Higher reactant concentrations and controlled pH can lead to more uniform and smaller NPs, while the temperature and rate of addition can influence the crystallinity and agglomeration of the particles.

In the hydrothermal method, temperature, pressure, type of solvent, and reaction time are critical factors. Higher temperatures and pressures generally produce better crystallinity and larger particles, while the choice of solvent can significantly influence the shape and size distribution of the NPs.

In the thermal decomposition method, the key parameters include temperature, heating rate, and the choice of precursor. Higher temperatures and controlled heating rates usually yield uniform particle sizes and higher purity. The type of precursor can determine the phase and morphology of the resulting NiO NPs, and faster heating rates often lead to smaller particles due to rapid nucleation.

For the sol–gel method, the concentration of precursors, pH of the sol, aging time, and drying conditions are crucial. Adjusting these parameters can lead to differences in particle size, morphology, and degree of agglomeration. Higher precursor concentrations or longer aging times typically result in larger particles and more defined crystalline structures.

In the microemulsion method, the water-to-surfactant ratio, type of surfactant, and reaction temperature are essential parameters. These factors control the size and shape of the NPs by influencing the size of the microemulsion droplets. Adjusting the water-to-surfactant ratio can fine-tune particle size, while different surfactants can stabilize droplets of various sizes and shapes.

Variations in these parameters influence the final product by altering nucleation and growth rates, particle size distribution, and surface characteristics, which in turn affect the physical and chemical properties of the NiO NPs. Postsynthesis processing techniques can markedly enhance the characteristics of NiO NPs. Annealing, a common technique across different synthesis methods, improves crystallinity, reduces defects, and enhances magnetic properties. Adjusting the annealing temperature and atmosphere (e.g., air, nitrogen, or reducing gases) allows one to tailor the NPs' characteristics. Surface functionalization, which involves modifying the NP surface with organic molecules, polymers, or other inorganic materials, enhances stability, dispersibility, and compatibility with other materials. This technique is particularly useful for biomedical applications where biocompatibility and functionalization with targeting molecules are crucial.

4. The Impact of Structural and Compositional Variations on the Magnetic Behavior of NiO NPs

The fascinating magnetic properties of NiO NPs have garnered significant attention due to their potential applications in various fields, such as spintronics, catalysis, and biomedicine [7–9]. Unlike their bulk counterparts, NiO NPs exhibit unique magnetic behavior primarily influenced by their reduced structure and tunned composition. In this section, the key aspects governing the magnetic properties of these systems are reviewed, including finite-size and surface effects, NP morphology, crystal quality, and the impact of the parasitic Ni phase.

4.1. Finite-Size and Surface Effects

The magnetic properties of NiO NPs differ significantly from bulk materials due to their increased surface-to-volume ratio, the presence of uncompensated spins either on the

surface or throughout the particle volume, and the effect of multiple sublattices at reduced sizes (see Figure 11) [1–3,24,26,32,42,90,91]. NiO NPs exhibit unique magnetic behaviors because of their smaller size and larger proportion of surface atoms. For instance, a 10 nm spherical NiO NP contains approximately 20% of its atoms on the surface, while smaller NPs, such as 5 nm spheres, have around 50% [4,80]. In these systems, the core typically exhibits AFM behavior, where the magnetic moments of nickel ions align AFM, resulting in a net zero magnetic moment. However, the surface of these systems can form an FM shell due to the presence of uncompensated spins (see Figure 11). This interaction between the FM shell and AFM core significantly alters the magnetic properties. Additionally, configurations of missing spins in NiO NPs can include randomly missing spins within the particle, on the surface, or due to an odd number of layers within a cubic structure. These phenomena lead to unique behaviors, such as reduced T_B and T_N, larger magnetic moments, and increased coercivities [32,35,42,90,92,93].

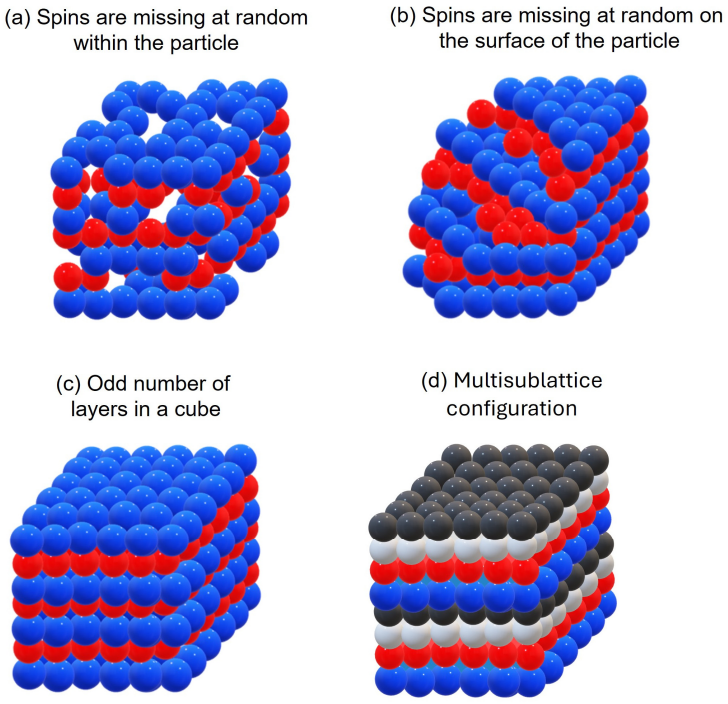

Figure 11. Configurations of spins in NiO NPs: (**a**) Randomly missing spins within the particle. (**b**) Randomly missing spins on the particle's surface. (**c**) Missing spins due to an odd number of layers within a cubic structure. (**d**) Multi-sub-lattice configuration of spins.

In their seminal work, Kodama et al. delved into the finite-size effects exhibited by NiO NPs [31], shedding light on their anomalous magnetic properties. By investigating particles with sizes ranging from 6 to 80 nm, synthesized through chemical precipitation followed by annealing, the study revealed intriguing phenomena. The magnetic moments observed in these NiO NPs exceeded the predictions of a conventional 2-sublattice AFM model. Instead, a novel finite-size effect emerged: the reduced coordination of surface spins led to changes in the magnetic order throughout the particle. Remarkably, NiO NPs exhibited 8-, 6-, or 4-sublattice spin configurations, deviating from the expected 2-sublattice model. These multi-sub-lattice arrangements resulted in high net moments and diverse spin reversal paths, contributing to large coercivities and hysteresis loop shifts of up to 10 kOe. As particle size decreased, the impact of uncompensated surface spins became more pronounced. Numerical modeling corroborated the notion that this behavior stems from reduced coordination among surface spins. Interestingly, the average order parameter approached unity as particle size increased, while the number of sublattices decreased from 8 to 2 in larger particles.

Surface spins played a crucial role, particularly at lower temperatures, where stronger interactions contributed to the observed magnetic behavior [36,42,72,90,92–94]. For example, Sharma et al. reported a magnetic surface contribution in 6 nm NiO NPs synthesized by a thermal decomposition route [36], finding that the interaction between the FM shell and the AFM core enhanced the overall particle magnetization. The synthesized NiO NPs exhibited a crystalline core and a broad disordered surface shell, accounting for about 75 ± 20% of the total particle diameter. As a result, magnetic behavior was dominated by significant surface effects, particularly at low temperatures. Key magnetic properties included shifted hysteresis loops, enhanced coercivity, high field irreversibility, and a vertical shift in the magnetization curves after FC.

Another interesting example reported by Rinaldi et al. investigated the impact of the particle surface in ultra-small NiO NPs with sizes below 10 nm synthesized via the pyrolysis of $Ni(NO_3)_2$ [90,94]. Their findings revealed that 2 nm NiO NPs exhibit a completely disordered magnetic state, while particles larger than 4 nm exhibit a core/shell structure, featuring an uncompensated AFM NiO core and a spin glass (SG) shell, resulting in a net magnetic moment (see Figure 12). This core(AFM)/shell(SG) morphology induced H_{eb} due to the exchange coupling between the SG shell spins and the uncompensated AFM core moments.

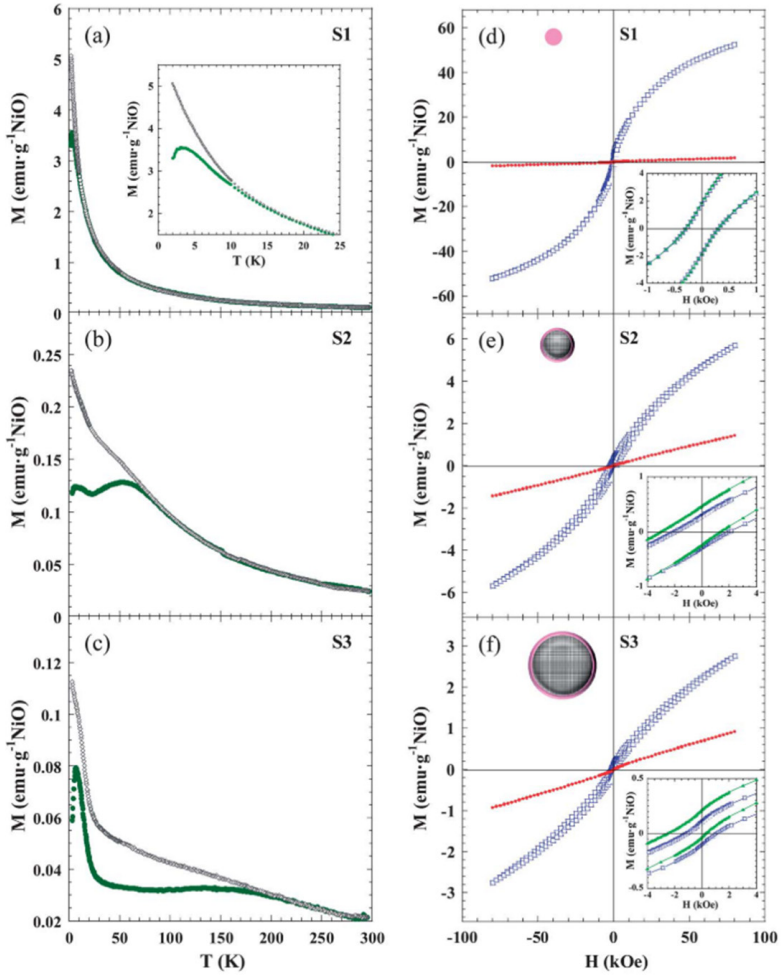

Figure 12. Size effects and magnetic properties of ultrasmall NiO NPs [90]: The left pane (**a**–**c**) shows the M_{ZFC}-M_{FC} curves from low to room temperature for NiO NPs with sample sizes ranging from 2 (S1) to 9 nm (S3). The inset in (**a**) shows the detail of M_{ZFC}-M_{FC} curves at low temperature. The right panel (**d**–**f**) shows the hysteresis loops at 2 K and 300 K of the same samples, represented by blue and red dots, respectively. Insets show the hysteresis loops measured after cooling samples from 300 K under an external field of 10 kOe (green triangles).

Particle size significantly impacts the magnetic properties, particularly M_{ZFC}-M_{FC} curves and hysteresis loops in these systems. The former measurements reveal an enhancement of T_B with the particle volume. Additionally, the peaks observed in the M_{ZFC} curves at low temperatures suggest spin-glass behavior probably due to surface effects. On the other hand, hysteresis loops exhibit two key trends. Smaller NiO NPs show significantly higher magnetization due to uncompensated surface spins, whereas larger particles display behaviors more characteristic of AFM materials. The hysteresis loops for smaller particles reveal large M_s at low temperatures, suggesting an FM-like behavior driven by surface effects. With rising temperatures, the coercivity diminishes, and the loops narrow, signaling a reduced impact of surface effects. These observations underscore the critical role of surface spin disorder and the effect of particle size reduction in enhancing the magnetic properties at lower temperatures in smaller NiO NPs. As the NiO NP size approaches the magnetic correlation length, surface spin disorder significantly influences the overall magnetic behavior. This disorder arises from the reduced coordination of surface atoms, bond relaxation, and increased static disorder, all of which weaken the exchange interactions necessary for maintaining AFM order. As a result, T_N exhibits an intrinsic size dependence, progressively decreasing with smaller NP diameters [33,35,68]. One significant study that sheds light on this phenomenon was conducted by Rinaldi et al. [68], who investigated the size-dependent reduction of T_N in small NiO NPs with average diameters ranging from 4 to 9 nm. Using neutron diffraction and X-ray absorption fine structure (EXAFS) measurements, they found that T_N decreases with reducing NP size. Specifically, T_N values decreased to 461 K for 4 nm particles, 497 K for 6 nm particles, 505 K for 7 nm particles, and 513 K for 9 nm particles. The observed variation was attributed to significant surface effects, including average undercoordination, bond relaxation, and static disorder, which collectively weaken the exchange interactions required for maintaining AFM order.

4.2. Impact of Structure and Coating on the Magnetic Behavior of NiO NPs

The magnetic properties of NiO NPs are significantly influenced by their morphology, as it directly affects surface area, surface energy, and the distribution of surface and bulk atoms—all of which play a role in determining magnetic behavior. Specific morphologies can either enhance or diminish magnetic interactions, resulting in diverse magnetic behaviors. Various shapes and structures, including nanorods [69], cuboctahedral [92], nanosheets [17], and branchlike forms [95] can lead to substantial variations in magnetic behavior. For example, Wesselinowa investigated the impact of particle size and anisotropy on the magnetic properties of cuboctahedral morphologies using a theoretical approach based on the Heisenberg model [92]. The study revealed that, as particle size decreases, magnetization increases due to enhanced surface spin contributions. H_c exhibited notable dependence on particle size and surface anisotropy, indicating that the shape and size of NPs play crucial roles in determining their magnetic properties. Additionally, T_N was found to decrease with decreasing particle size, linked to surface effects and reduced symmetry at the nanoscale.

Zhao, Yang, and Hua reported the synthesis and magnetic properties of 100 nm β-$Ni(OH)_2$ and NiO nanosheets [17]. The β-$Ni(OH)_2$ nanosheets, synthesized via a hydrothermal method, displayed FM behavior at low temperature around 5 K and paramagnetic behavior at 300 K. Upon thermal decomposition of β-$Ni(OH)_2$ at 450 °C, NiO nanosheets were formed, exhibiting T_B greater than room temperature and nonzero values of H_c even at 300 K.

Liu, Li, and Yang reported size-dependent magnetic properties of branchlike NiO NPs synthesized via the thermal decomposition of nickel(II) acetate in the presence of organic surfactants [95]. The resulting NiO nanocrystals ranged from 5 nm to 13 nm in size, demonstrating that both size and morphology significantly influence their magnetic properties. These branchlike structures exhibited higher M_r and H_c compared with spherical counterparts, attributed to their larger surface-to-volume ratio and an increased number of uncompensated surface spins. This unique two-dimensional nanosheet structure also affected magnetization relaxation processes, highlighting the critical role of the NP shape

in determining magnetic properties. Additionally, they found that particles smaller than 13 nm exhibited weak FM behavior at room temperature due to uncompensated surface spins. Both average T_B and irreversibility temperature increased with particle size, while M_r and H_c at 300 K decreased with increasing particle size, emphasizing the significant role of surface effects in smaller particles.

The particle coating plays a crucial role in modulating the magnetic properties of NiO NPs by mitigating interparticle interactions and stabilizing surface spins, influencing T_B accordingly [65,93]. For example, Shim et al. investigated the size dependence of T_B and electron magnetic resonance (EMR) spectra in NiO NPs with sizes ranging from 5 to 20 nm [93]. In the study, both uncoated and oleic acid-coated (OA) NiO NPs were synthesized using annealing methods. The research revealed that uncoated NiO NPs exhibited higher T_B compared with OA-coated NPs, suggesting significant interparticle interactions in the uncoated samples. Key findings included the linear variation in T_B with NP volume for OA-coated NPs, indicating negligible interparticle interactions. In contrast, uncoated NPs showed increased T_B with decreasing size for NPs smaller than 8 nm, attributed to enhanced interparticle interactions. Figure 13 depicts the M_{ZFC}-M_{FC} curves of both uncoated and coated 7 nm NiO NPs, revealing a shift to lower T_B from 170 to 55 K for uncoated and OA-coated NiO NPs, respectively. Besides, K_{eff} increased with decreasing particle size, reflecting enhanced surface anisotropy contributions in smaller NPs. Finally, H_c and H_{eb} measurements revealed that smaller particles exhibited higher H_c probably due to greater surface anisotropy and uncompensated surface spins, with significant H_{eb} values suggesting strong interactions between the FM-like surface spins and the AFM core.

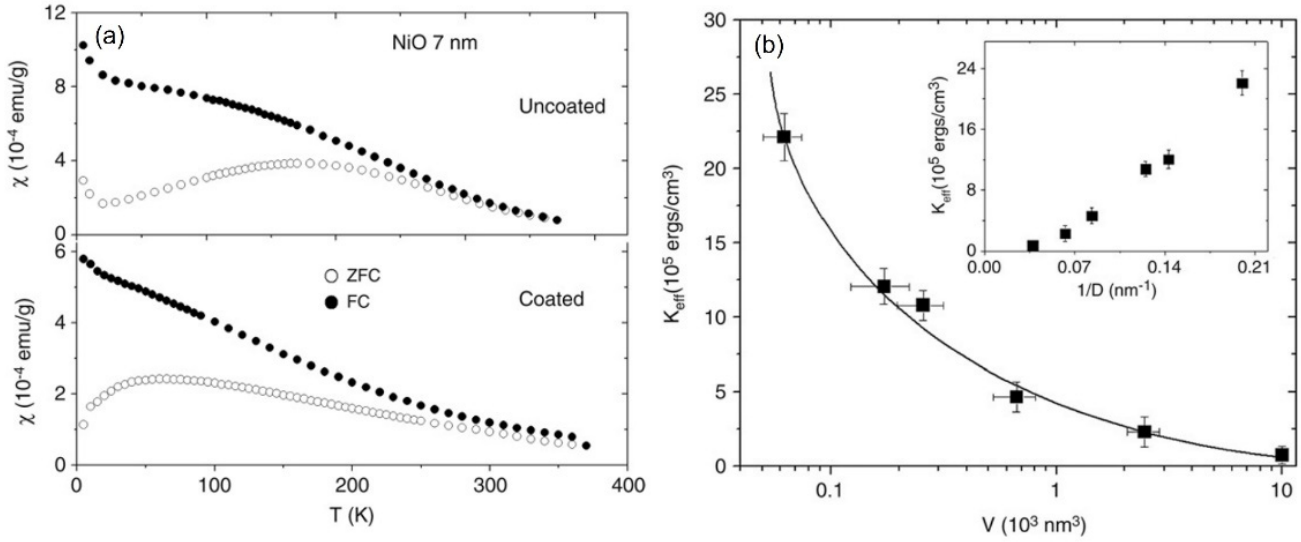

Figure 13. (**a**) Comparison of the M_{ZFC}-M_{FC} curves for uncoated and OA-coated 7 nm NiO NPs. (**b**) Variation in K_{eff} with particle volume (V) of the coated NiO NPs derived from the data analysis. In the inset, the nonlinear variation in K_{eff} with $1/D$ is evident [93].

4.3. Influence of Oxygen Stoichiometry and Metallic Nickel Presence on the Magnetic Properties of NiO NPs

The stoichiometry of NiO NPs significantly influences its magnetic and electronic properties. Dubey et al. investigated this effect on the magnetic and electronic properties of NiO NPs prepared through the thermal decomposition of $Ni(NO_3)_2 \cdot 6H_2O$ at various sintering temperatures ranging from 400 °C to 1100 °C [37]. The study revealed how varying levels of excess oxygen impact these properties. For example, the magnetic susceptibility and specific heat capacity measurements indicated a shift in T_N with changes in stoichiometry. Besides, NiO samples sintered at 400 °C exhibited higher levels of excess oxygen and a corresponding lower T_N. In contrast, samples sintered at the highest temperatures of 1100 °C, had lower excess oxygen levels and higher T_N. Additionally, XPS revealed a higher

concentration of Ni^{3+} ions in samples sintered at lower temperatures, indicating a higher degree of nonstoichiometry. This transition from Ni^{2+} to Ni^{3+} with increasing sintering temperature affects the magnetic properties due to modifications in the Ni-O bond length and Ni-O-Ni bond angle.

The presence and distribution of Ni within the NiO structure significantly influence the magnetic properties of NiO NPs. For example, Chaghouri et al. investigated the magnetic properties of Ni/NiO nanocrystals [96], focusing on the effects of exchange bias. In the study, Ni/NiO nanocrystals were synthesized by annealing Ni NPs coated with a thin amorphous NiO layer, resulting in nanocrystals with diameters ranging from 5.0 to 16.8 nm. Magnetic measurements showed that the smaller particles exhibited robust room temperature FM with strong exchange bias. M_{ZFC}-M_{FC} curves indicated a clear transition to FM order at 300 K, with $M_s = 15.8$ emu/g and $H_c = 228$ Oe. The occurrence of H_{eb} was confirmed by a hysteresis loop shift of 62 Oe at room temperature, which increased significantly at 2 K with higher cooling fields. The annealing process, which induced crystallization of the NiO shell and increased oxidation of the Ni core, preserved and enhanced exchange bias features. H_{eb} increased with particle size, from 34 Oe for 5.0 nm particles to 194 Oe for 16.8 nm particles, and H_c values were higher than those previously reported for Ni/NiO systems.

Another interesting example was reported by Rostamnejadi et al. [10], who investigated the magnetic properties of Ni/NiO NPs, synthesized by the sol–gel method. The study found that Ni/NiO nanocomposites exhibit FM behavior at room temperature, which is unusual for AFM NiO. The observed FM moment was primarily attributed to uncompensated surface spins and FM clusters within the AFM NiO matrix. Magnetic hysteresis loops revealed that M_s of the samples sintered at 450 °C (34 nm) and 550 °C (40 nm) were 3.5 emu/g and 0.2 emu/g, respectively. Interestingly, H_c values were low for both samples, with 94 Oe for S1 and 95 Oe for S2, indicating the presence of weak FM phases.

4.4. Outlook on the Impact of Structural and Compositional Variations on the Magnetic Behavior of NiO NPs

To recapitulate, NiO NPs exhibit distinctive magnetic behaviors influenced by their structural and compositional characteristics. Key factors such as finite-size effects, surface effects, morphology, crystal quality, the presence of different phases of Ni, and impurities play crucial roles in determining the magnetic properties of these systems.

Finite-size effects in NiO NPs arise from the reduced dimensions of the particles, leading to unique magnetic properties compared with bulk materials. These effects are due to uncompensated spins within the particle volume, the presence of odd sublattices, and the formation of multiple sublattices that yield nonzero magnetization. Smaller particles, for instance, display larger magnetic moments and enhanced H_c because of these finite-size effects. As particle size decreases, the influence of these internal spins becomes more prominent, resulting in significant deviations from the typical AFM behavior of bulk NiO.

Surface effects, on the other hand, are primarily due to the high surface-to-volume ratio in NiO NPs, where numerous uncompensated spins on the surface lead to a net magnetic moment. Surface defects, such as vacancies or interstitials, can create uncompensated spins, leading to FM behavior in otherwise AFM materials. The high proportion of surface atoms in NiO NPs results in FM order due to these spins. This FM shell interacts with the AFM core, changing the overall magnetic properties, especially in smaller particles, leading to increased H_c and larger magnetic moments. The core–shell structures that form in smaller NPs exhibit AFM behavior in the core and FM signatures in the surface shell.

The magnetic properties are also highly dependent on the morphology of the NPs. Different shapes, such as nanorods, cuboctahedral, nanosheets, and branch-like structures, exhibit varying magnetic behaviors due to differences in surface area and anisotropy. Specific morphologies can enhance surface spin contributions, leading to increased magnetization and H_c. For instance, branch-like NiO structures demonstrate higher M_r and

H_c compared with spherical counterparts due to their larger surface-to-volume ratios and uncompensated surface spins.

Coating the NPs, such as with oleic acid, can significantly modulate their magnetic properties by reducing interparticle interactions and stabilizing surface spins. Coated NPs generally exhibit lower T_B compared with uncoated ones, indicating that coatings can effectively diminish magnetic interactions between particles. Additionally, coatings and functionalization of the NP surface can stabilize defects and further modify the magnetic properties.

The stoichiometry of NiO NPs, including the presence of excess oxygen and variations in the nickel oxidation state, plays a crucial role in their magnetic behavior. Changes in stoichiometry can alter the T_N and the overall magnetic order, as seen in NPs sintered at different temperatures. The presence of metallic Ni within the NiO matrix can also induce FM behavior, further complicating the magnetic landscape of these systems.

Impurities also affect magnetic properties by introducing foreign atoms or ions that change magnetic interactions within the NiO structure. Introducing FM impurities like Ni or Fe can enhance the FM character of the particles, increasing both M_s and H_{eb}. This can be particularly interesting in applications such as magnetic storage devices and spintronic components, where improved magnetic properties are crucial.

These defects and impurities can be introduced through various synthesis methods and postsynthesis treatments. By controlling synthesis parameters like temperature, precursor concentration, and annealing conditions, it is possible to adjust the degree and type of defects and impurities. For instance, annealing NiO NPs at different temperatures can vary oxygen vacancies, affecting the magnetic properties. Lower annealing temperatures generally result in higher defect levels, leading to increased FM behavior due to more uncompensated spins.

5. Conclusions and Perspectives

Research on NiO NPs is a promising frontier in material science, with significant implications for various advanced applications. Their unique magnetic properties, distinct from bulk materials, offer numerous opportunities and challenges for future research and technological innovations. Understanding surface effects is crucial, as uncompensated surface spins significantly influence the magnetic properties of NiO NPs. Future research should focus on elucidating the mechanisms governing surface spin interactions and their impact on overall magnetic behavior. Advanced characterization techniques, such as spin-polarized scanning tunneling microscopy, X-ray absorption spectroscopy, X-ray magnetic linear dichroism, and photoemission electron microscopy could provide detailed insights into these phenomena.

Tuning magnetic properties through size and morphology offers a pathway to tailor NiO NPs for specific applications. Systematic studies on anisotropic morphologies, such as nanostars, nanorods, and nanoflowers, could lead to NPs optimized for targeted uses. Additionally, exploring the impact of stoichiometry and dopants on the magnetic properties of NiO NPs could identify optimal doping strategies that enhance performance while maintaining stability.

The exchange bias effect observed in Ni/NiO core/shell structures opens new possibilities for spintronic devices. Investigating the stability and tunability of this effect at room temperature and under varying environmental conditions could pave the way for robust and efficient spintronic components. Controlling the core/shell ratio and interface quality will be crucial.

Another promising area is bio-inspired green synthesis, which utilizes natural materials and processes to create NiO NPs in an environmentally friendly manner. For instance, the use of plant extracts as reducing and capping agents can simplify the synthesis process and make it more sustainable [9,74,80,82]. Such green synthesis methods have already shown potential in producing NiO NPs with desirable properties for various applications.

In biomedicine, NiO NPs show significant promise due to their ability to generate reactive oxygen species, making them effective as antimicrobial and anticancer agents. Their high surface area and reactivity enable them to target and destroy pathogens and cancer cells, paving the way for innovative treatments and drug delivery systems [13,44,91].

Furthermore, the combination of NiO NPs with other magnetic materials can lead to the development of advanced FM and AFM composites. These composites are particularly valuable in spintronic devices, where the unique magnetic properties of NiO NPs can be utilized to enhance performance and functionality. Studies have demonstrated the potential of integrating NiO with ZnO, which affects magnetic behavior and opens new avenues for creating customized magnetic materials.

Overall, finely tuning the magnetic properties of NiO NPs through careful control of their size, shape, composition, and surface characteristics is key to unlocking their full potential in applications such as spintronics, catalysis, and biomedicine.

Author Contributions: Conceptualization, C.M.; writing—original draft preparation, C.M., J.A., A.L. and X.B.; revision, C.M., J.A., A.L. and X.B. All authors have read and agreed to the published version of the manuscript.

Funding: This research was funded by the Spanish Ministry of Science and Innovation (MICIIN) under grant numbers PGC2018-097789-B-I00 and PID2021-127397NB-I00, the Catalan Agency for Management of University and Research Grants (AGAUR) through the Groups of Excellence program (2021SGR00328), and the European Union's FEDER funds.

Institutional Review Board Statement: Not applicable.

Informed Consent Statement: Not applicable.

Data Availability Statement: No new data were generated in this study.

Acknowledgments: C.M. acknowledges the funding support from the University of Barcelona and the Spanish Ministry of Universities under the program Maria Zambrano Program founded by the European Union Next Generation-EU/PRTR and the Beatriu de Pinós fellowship program with the number 2022 BP 00243.

Conflicts of Interest: The authors declare no conflicts of interest.

References

1. Cullity, B.D.; Graham, C.D. *Introduction to Magnetic Materials*; John Wiley & Sons: Hoboken, NJ, USA, 2011; ISBN 1118211499.
2. Batlle, X.; Labarta, A. Finite-Size Effects in Fine Particles: Magnetic and Transport Properties. *J. Phys. D Appl. Phys.* **2002**, *35*, 15–42.
3. Liu, X.; Wang, K. Antiferromagnetic Materials and Their Manipulations. In *Spintronics: Materials, Devices and Applications*; Wiley Online Library: Hoboken, NJ, USA, 2022; ISBN 978-1119698975.
4. Batlle, X.; Moya, C.; Escoda-Torroella, M.; Iglesias, Ò.; Fraile Rodríguez, A.; Labarta, A. Magnetic Nanoparticles: From the Nanostructure to the Physical Properties. *J. Magn. Magn. Mater.* **2022**, *543*, 168594. [CrossRef]
5. Müller, K.H.; Sawatzki, S.; Gauß, R.; Gutfleisch, O. *Permanent Magnet Materials and Applications in Handbook of Magnetism and Magnetic Materials*; Springer International Publishing: Cham, Switzerland, 2021; ISBN 9783030632083.
6. Ali, A.; Shah, T.; Ullah, R.; Zhou, P.; Guo, M.; Ovais, M.; Tan, Z.; Rui, Y.K. Review on Recent Progress in Magnetic Nanoparticles: Synthesis, Characterization, and Diverse Applications. *Front. Chem.* **2021**, *9*, 629054. [CrossRef]
7. Bonomo, M. Synthesis and Characterization of NiO Nanostructures: A review. *J. Nanopart. Res.* **2018**, *20*, 222. [CrossRef]
8. Narender, S.S.; Varma, V.V.S.; Srikar, C.S.; Ruchitha, J.; Varma, P.A.; Praveen BV, S. Nickel Oxide Nanoparticles: A Brief Review of Their Synthesis, Characterization, and Applications. *Chem. Eng. Technol.* **2022**, *45*, 397–409. [CrossRef]
9. Ahmad, W.; Chandra Bhatt, S.; Verma, M.; Kumar, V.; Kim, H. A Review on Current Trends in the Green Synthesis of Nickel Oxide Nanoparticles, Characterizations, and Their Applications. *Environ. Nanotechnol. Monit. Manag.* **2022**, *18*, 100674. [CrossRef]
10. Rostamnejadi, A.; Bagheri, S. Optical, Magnetic, and Microwave Properties of Ni/NiO Nanoparticles. *Appl. Phys. A Mater. Sci. Process.* **2017**, *123*, 233. [CrossRef]
11. Hugel, J.; Carabatos, C. Band Structure and Optical Properties of NiO. I. Band Structure Calculations. *J. Phys. C Solid State Phys.* **1983**, *16*, 6713. [CrossRef]
12. Tian, J.; Shao, Q.; Dong, X.; Zheng, J.; Pan, D.; Zhang, X.; Cao, H.; Hao, L.; Liu, J.; Mai, X.; et al. Bio-Template Synthesized NiO/C Hollow Microspheres with Enhanced Li-Ion Battery Electrochemical Performance. *Electrochim. Acta* **2018**, *261*, 236–245. [CrossRef]
13. Kannan, K.; Radhika, D.; Sadasivuni, K.K.; Reddy, K.R.; Raghu, A.V. Nanostructured Metal Oxides and Its Hybrids for Photocatalytic and Biomedical Applications. *Adv. Colloid Interface Sci.* **2020**, *281*, 102178. [CrossRef]

14. Ata-ur-Rehman; Iftikhar, M.; Latif, S.; Jevtovic, V.; Ashraf, I.M.; El-Zahhar, A.A.; Abdu Musad Saleh, E.; Mustansar Abbas, S. Current Advances and Prospects in NiO-Based Lithium-Ion Battery Anodes. *Sustain. Energy Technol. Assess.* **2022**, *53*, 102376. [CrossRef]
15. Spinner, N.S.; Palmieri, A.; Beauregard, N.; Zhang, L.; Campanella, J.; Mustain, W.E. Influence of Conductivity on the Capacity Retention of NiO Anodes in Li-Ion Batteries. *J. Power Sources* **2015**, *276*, 46–53. [CrossRef]
16. Fan, Z.; Liang, J.; Yu, W.; Ding, S.; Cheng, S.; Yang, G.; Wang, Y.; Xi, Y.; Xi, K.; Kumar, R.V. Ultrathin NiO Nanosheets Anchored on a Highly Ordered Nanostructured Carbon as an Enhanced Anode Material for Lithium Ion Batteries. *Nano Energy* **2015**, *16*, 152–162. [CrossRef]
17. Wu, X.; Li, S.; Xu, Y.; Wang, B.; Liu, J.; Yu, M. Hierarchical Heterostructures of NiO Nanosheet Arrays Grown on Pine Twig-like B-NiS@Ni3S2 Frameworks as Free-Standing Integrated Anode for High-Performance Lithium-Ion Batteries. *Chem. Eng. J.* **2019**, *356*, 245–254. [CrossRef]
18. Sivagami, M.; Asharani, I.V. Phyto-Mediated Ni/NiO NPs and Their Catalytic Applications-a Short Review. *Inorg. Chem. Commun.* **2022**, *145*, 110054. [CrossRef]
19. Delgado, D.; Sanchis, R.; Solsona, B.; Concepción, P.; López Nieto, J.M. Influence of the Nature of the Promoter in NiO Catalysts on the Selectivity to Olefin During the Oxidative Dehydrogenation of Propane and Ethane. *Top. Catal.* **2020**, *63*, 1731–1742. [CrossRef]
20. Abbas, S.A.; Iqbal, M.I.; Kim, S.H.; Jung, K.D.; Shim, H.; Dutta, P.; Seehra, M.S.; Bonevich, J.; Jafari, A.; Pilban Jahromi, S.; et al. Catalytic Activity of Urchin-like Ni Nanoparticles Prepared by Solvothermal Method for Hydrogen Evolution Reaction in Alkaline Solution. *Electrochim. Acta* **2017**, *227*, 382–390. [CrossRef]
21. Silva, T.L.; Meinerz, V.H.; Vidart, J.M.M.; Gimenes, M.L.; Vieira, M.G.A.; Silva, M.G.C. Metallic Affinity of Toxic and Noble Metals by Particles Produced from Sericin, Alginate and Poly-(Ethylene Glycol). *Chem. Eng. Trans.* **2017**, *56*, 1903–1908.
22. Li, Q.; Zeng, W.; Li, Y. NiO-Based Gas Sensors for Ethanol Detection: Recent Progress. *J. Sens.* **2022**, *2022*, 1855493. [CrossRef]
23. Din, S.U.; Iqbal, H.; Haq, S.; Ahmad, P.; Khandaker, M.U.; Elansary, H.O.; Al-Harbi, F.F.; Abdelmohsen, S.A.M.; Zin El-Abedin, T.K. Investigation of the Biological Applications of Biosynthesized Nickel Oxide Nanoparticles Mediated by Buxus Wallichiana Extract. *Crystals* **2022**, *12*, 146. [CrossRef]
24. Isa khan, M.; Nawaz, M.; Bilal Tahir, M.; Iqbal, T.; Pervaiz, M.; Rafique, M.; Aziz, F.; Younas, U.; Alrobei, H. Synthesis, Characterization and Antibacterial Activity of NiO NPs against Pathogen. *Inorg. Chem. Commun.* **2020**, *122*, 108300. [CrossRef]
25. Anand, G.T.; Nithiyavathi, R.; Ramesh, R.; John Sundaram, S.; Kaviyarasu, K. Structural and Optical Properties of Nickel Oxide Nanoparticles: Investigation of Antimicrobial Applications. *Surf. Interfaces* **2020**, *18*, 100460. [CrossRef]
26. Moriyama, T.; Oda, K.; Ohkochi, T.; Kimata, M.; Ono, T. Spin Torque Control of Antiferromagnetic Moments in NiO. *Sci. Rep.* **2018**, *8*, 14167. [CrossRef] [PubMed]
27. Kwon, U.; Kim, B.G.; Nguyen, D.C.; Park, J.H.; Ha, N.Y.; Kim, S.J.; Ko, S.H.; Lee, S.; Lee, D.; Park, H.J. Solution-Processible Crystalline NiO Nanoparticles for High-Performance Planar Perovskite Photovoltaic Cells. *Sci. Rep.* **2016**, *6*, 30759. [CrossRef]
28. Kuwa, M.; Harada, M.; Sato, R.; Teranishi, T. Ligand-Stabilized CoO and NiO Nanoparticles for Spintronic Devices with Antiferromagnetic Insulators. *ACS Appl. Nano Mater.* **2020**, *3*, 2745–2755. [CrossRef]
29. Gandhi, A.C.; Pradeep, R.; Yeh, Y.C.; Li, T.Y.; Wang, C.Y.; Hayakawa, Y.; Wu, S.Y. Understanding the Magnetic Memory Effect in Fe-Doped NiO Nanoparticles for the Development of Spintronic Devices. *ACS Appl. Nano Mater.* **2019**, *2*, 278–290. [CrossRef]
30. Néel, L. Antiferromagnetism and Ferrimagnetism. *Proc. Phys. Soc. Sect. A* **1952**, *65*, 869–885. [CrossRef]
31. Kodama, R.H.; Makhlouf, S.A.; Berkowitz, A.E. Size Effects in Antiferromagnetic NiO Nanoparticles. *Phys. Rev. Lett.* **1997**, *79*, 1393–1396. [CrossRef]
32. Proenca, M.P.; Sousa, C.T.; Pereira, A.M.; Tavares, P.B.; Ventura, J.; Vazquez, M.; Araujo, J.P. Size and Surface Effects on the Magnetic Properties of NiO Nanoparticles. *Phys. Chem. Chem. Phys.* **2011**, *13*, 9561–9567.
33. Tadic, M.; Nikolic, D.; Panjan, M.; Blake, G.R. Magnetic Properties of NiO (Nickel Oxide) Nanoparticles: Blocking Temperature and Neel Temperature. *J. Alloys Compd.* **2015**, *647*, 1061–1068. [CrossRef]
34. Jafari, A.; Pilban Jahromi, S.; Boustani, K.; Goh, B.T.; Huang, N.M. Evolution of Structural and Magnetic Properties of Nickel Oxide Nanoparticles: Influence of Annealing Ambient and Temperature. *J. Magn. Magn. Mater.* **2019**, *469*, 383–390. [CrossRef]
35. Cooper, J.F.K.; Ionescu, A.; Langford, R.M.; Ziebeck, K.R.A.; Barnes, C.H.W.; Gruar, R.; Tighe, C.; Darr, J.A.; Thanh, N.T.K.; Ouladdiaf, B. Core/Shell Magnetism in NiO Nanoparticles. *J. Appl. Phys.* **2013**, *114*, 083906. [CrossRef]
36. Sharma, S.K.; Vargas, J.M.; De Biasi, E.; Béron, F.; Knobel, M.; Pirota, K.R.; Meneses, C.T.; Kumar, S.; Lee, C.G.; Pagliuso, P.G.; et al. The Nature and Enhancement of Magnetic Surface Contribution in Model NiO Nanoparticles. *Nanotechnology* **2010**, *21*, 035602. [CrossRef]
37. Dubey, P.; Kaurav, N.; Devan, R.S.; Okram, G.S.; Kuo, Y.K. The Effect of Stoichiometry on the Structural, Thermal and Electronic Properties of Thermally Decomposed Nickel Oxide. *RSC Adv.* **2018**, *8*, 5882–5890. [CrossRef] [PubMed]
38. Rooksby, H.P. Structure of Nickel Oxide. *Nature* **1943**, *152*, 304. [CrossRef]
39. Gomonay, O.; Bossini, D. Spin Dynamics in Antiferromagnets. *J. Phys. D Appl. Phys.* **2021**, *54*, 374004. [CrossRef]
40. Arai, K.; Okuda, T.; Tanaka, A.; Kotsugi, M.; Fukumoto, K.; Ohkochi, T.; Nakamura, T.; Matsushita, T.; Muro, T.; Oura, M.; et al. Collinear Spin Structure in NiO: Antiferromagnetic Superexchange Interaction and Magnetostriction. *Phys. Rev. B* **2012**, *85*, 104418. [CrossRef]

41. Adiba; Pandey, V.; Munjal, S.; Ahmad, T. Structural, Morphological and Magnetic Properties of Antiferromagnetic Nickel Oxide Nanoparticles Synthesized via Sol-Gel Route. *Mater. Today Proc.* **2019**, *26*, 3116–3118.
42. Popkov, S.I.; Krasikov, A.A.; Dubrovskiy, A.A.; Volochaev, M.N.; Kirillov, V.L.; Martyanov, O.N.; Balaev, D.A. Size Effects in the Formation of an Uncompensated Ferromagnetic Moment in NiO Nanoparticles. *J. Appl. Phys.* **2019**, *126*, 103904. [CrossRef]
43. Kramers, H.A. Théorie Générale de La Rotation Paramagnétique Dans Les Cristaux. *Proc. Acad. Amst.* **1930**, *33*, 959–972.
44. Sandler, S.E.; Fellows, B.; Thompson Mefford, O. Best Practices for Characterization of Magnetic Nanoparticles for Biomedical Applications. *Anal. Chem.* **2019**, *91*, 14159–14169. [CrossRef]
45. Bean, C.P.; Livingston, J.D. Superparamagnetism. *J. Appl. Phys.* **1959**, *30*, S120. [CrossRef]
46. Batlle, X.; Obradors, X.; Medarde, M.; Rodríguez-Carvajal, J.; Pernet, M.; Vallet-Regí, M. Surface Spin Canting in $BaFe_{12}O_{19}$ Fine Particles. *J. Magn. Magn. Mater.* **1993**, *124*, 228–238. [CrossRef]
47. Batlle, X.; Garcia del Muro, M.; Tejada, J.; Pfeiffer, H.; Garnett, P.; Sinn, E. Magnetic Study of M-Type Doped Barium Ferrite Nanocrystalline Powders. *J. Appl. Phys.* **1993**, *74*, 3333. [CrossRef]
48. Moya, C.; Iglesias, Ó.; Batlle, X.; Labarta, A. Quantification of Dipolar Interactions in $Fe_{3-X}O_4$ Nanoparticles. *J. Phys. Chem. C* **2015**, *119*, 24142–24148. [CrossRef]
49. Anjum, D.H. Characterization of Nanomaterials with Transmission Electron Microscopy. In *IOP Conference Series: Materials Science and Engineering*; IOP Publishing: Bristol, UK, 2016; Volume 146.
50. Lee, B.; Yoon, S.; Lee, J.W.; Kim, Y.; Chang, J.; Yun, J.; Ro, J.C.; Lee, J.S.; Lee, J.H. Statistical Characterization of the Morphologies of Nanoparticles through Machine Learning Based Electron Microscopy Image Analysis. *ACS Nano* **2020**, *14*, 17125–17133. [CrossRef]
51. Smith, D.J. Characterization of Nanomaterials Using Transmission Electron Microscopy. In *Nanocharacterisation*; Kirkland, A.I., Haigh, S.J., Eds.; Royal Society of Chemistry: Cambridge, UK, 2015; pp. 1–29. ISBN 978-1-84973-805-7.
52. Schneider, C.A.; Rasband, W.S.; Eliceiri, K.W. NIH Image to ImageJ: 25 Years of Image Analysis. *Nat. Methods* **2012**, *9*, 671–675. [CrossRef] [PubMed]
53. Escoda-Torroella, M.; Moya, C.; Rodríguez, A.F.; Batlle, X.; Labarta, A. Selective Control over the Morphology and the Oxidation State of Iron Oxide Nanoparticles. *Langmuir* **2021**, *37*, 35–45. [CrossRef]
54. Kiss, L.B.; Söderlund, J.; Niklasson, G.A.; Granqvist, C.G. New Approach to the Origin of Lognormal Size Distributions of Nanoparticles. *Nanotechnology* **1999**, *10*, 25–28. [CrossRef]
55. Phakatkar, A.H.; Shokuhfar, T.; Shahbazian-Yassar, R. Nanoscale Chemical and Structural Investigation of Solid Solution Polyelemental Transition Metal Oxide Nanoparticles. *iScience* **2023**, *26*, 106032. [CrossRef]
56. Vladár, A.E.; Hodoroaba, V.-D. Characterization of Nanoparticles by Scanning Electron Microscopy. In *Characterization of Nanoparticles: Measurement Processes for Nanoparticles*; Hodoroaba, V.-D., Unger, W., Shard, A., Eds.; Elsevier: Amsterdam, The Netherlands, 2020; pp. 7–27. ISBN 978-0-12-814182-3.
57. Holder, C.F.; Schaak, R.E. Tutorial on Powder X-Ray Diffraction for Characterizing Nanoscale Materials. *ACS Nano* **2019**, *13*, 7359–7365. [CrossRef]
58. Holzwarth, U.; Gibson, N. The Scherrer Equation versus the "Debye-Scherrer Equation". *Nat. Nanotechnol.* **2011**, *6*, 534. [CrossRef] [PubMed]
59. Rietveld, H.M. A Profile Refinement Method for Nuclear and Magnetic Structures. *J. Appl. Crystallogr.* **1969**, *2*, 65–71. [CrossRef]
60. Grosvenor, A.P.; Biesinger, M.C.; Smart, R.S.C.; McIntyre, N.S. New Interpretations of XPS Spectra of Nickel Metal and Oxides. *Surf. Sci.* **2006**, *600*, 1771–1779. [CrossRef]
61. Peck, M.A.; Langell, M.A. Comparison of Nanoscaled and Bulk NiO Structural and Environmental Characteristics by XRD, XAFS, and XPS. *Chem. Mater.* **2012**, *24*, 4483–4490. [CrossRef]
62. Chastain, J.; King, R.C., Jr. *Handbook of X-ray Photoelectron Spectroscopy*; Perkin-Elmer Corporation: Waltham, MA, USA, 1992; ISBN 0962702625.
63. Khashan, K.S.; Sulaiman, G.M.; Hamad, A.H.; Abdulameer, F.A.; Hadi, A. Generation of NiO Nanoparticles via Pulsed Laser Ablation in Deionised Water and Their Antibacterial Activity. *Appl. Phys. A Mater. Sci. Process.* **2017**, *123*, 190. [CrossRef]
64. Das, S.; Kumar, A.; Singh, J.; Kumar, M. Fabrication and Modeling of Laser Ablated NiO Nanoparticles Decorated SnO_2 Based Formaldehyde Sensor. *Sens. Actuators B Chem.* **2023**, *387*, 133824. [CrossRef]
65. Sherif El-Eskandarany, M.; Al-Hazza, A.; Al-Hajji, L.A.; Ali, N.; Al-Duweesh, A.A.; Banyan, M.; Al-Ajmi, F. Mechanical Milling: A Superior Nanotechnological Tool for Fabrication of Nanocrystalline and Nanocomposite Materials. *Nanomaterials* **2021**, *11*, 2484. [CrossRef]
66. Bizyaev, D.A.; Bukharaev, A.A.; Lebedev, D.V.; Nurgazizov, N.I.; Khanipov, T.F. Nickel Nanoparticles and Nanowires Obtained by Scanning Probe Lithography Using Point Indentation Technique. *Tech. Phys. Lett.* **2012**, *38*, 645–648. [CrossRef]
67. Mohseni Meybodi, S.; Hosseini, S.A.; Rezaee, M.; Sadrnezhaad, S.K.; Mohammadyani, D. Synthesis of Wide Band Gap Nanocrystalline NiO Powder via a Sonochemical Method. *Ultrason. Sonochem.* **2012**, *19*, 841–845.
68. Rinaldi-Montes, N.; Gorria, P.; Martínez-Blanco, D.; Fuertes, A.B.; Puente-Orench, I.; Olivi, L.; Blanco, J.A. Size Effects on the Neél Temperature of Antiferromagnetic NiO Nanoparticles. *AIP Adv.* **2016**, *6*, 056104. [CrossRef]
69. Seehra, M.S.; Shim, H.; Dutta, P.; Manivannan, A.; Bonevich, J. Interparticle Interaction Effects in the Magnetic Properties of NiO Nanorods. *J. Appl. Phys.* **2005**, *97*, 2003–2006. [CrossRef]

70. Ascencio, F.; Bobadilla, A.; Escudero, R. Study of NiO Nanoparticles, Structural and Magnetic Characteristics. *Appl. Phys. A Mater. Sci. Process.* **2019**, *125*, 279. [CrossRef]
71. Liu, P.; Ming, V.; Ng, H.; Yao, Z.; Zhou, J.; Lei, Y.; Yang, Z.; Lv, H.; Kong, L.B. Facile Synthesis and Hierarchical Assembly of Flower-like NiO Structures with Enhanced Dielectric and Microwave Absorption Properties. *ACS Appl. Mater. Interfaces* **2017**, *9*, 16404–16416. [CrossRef] [PubMed]
72. Rahal, H.T.; Awad, R.; Abdel-Gaber, A.M.; Bakeer, D.E.S. Synthesis, Characterization, and Magnetic Properties of Pure and EDTA-Capped NiO Nanosized Particles. *J. Nanomater.* **2017**, *2017*, 7460323. [CrossRef]
73. Patil, S.; Jagadale, S. *Co-Precipitation Methods for the Synthesis of Metal Oxide Nanostructures*, 1st ed.; Elsevier Ltd.: Amsterdam, The Netherlands, 2023; ISBN 9780128243534.
74. Zenkin, K.; Durmuş, S.; Emre, D.; Bilici, A.; Yılmaz, S. Salvia Officinalis Leaf Extract-Stabilized NiO NPs, ZnO NPs, and NiO@ZnO Nanocomposite: Green Hydrothermal Synthesis, Characterization and Supercapacitor Application. *Biomass Convers. Biorefinery* **2024**, *14*, 355–365.
75. Farhadi, S.; Roostaei-Zaniyani, Z. Preparation and Characterization of NiO Nanoparticles from Thermal Decomposition of the $[Ni(En)_3](NO_3)_2$ Complex: A Facile and Low-Temperature Route. *Polyhedron* **2011**, *30*, 971–975. [CrossRef]
76. Ibrahim, E.M.M.; Abdel-Rahman, L.H.; Abu-Dief, A.M.; Elshafaie, A.; Hamdan, S.K.; Ahmed, A.M. The Synthesis of CuO and NiO Nanoparticles by Facile Thermal Decomposition of Metal-Schiff Base Complexes and an Examination of Their Electric, Thermoelectric and Magnetic Properties. *Mater. Res. Bull.* **2018**, *107*, 492–497. [CrossRef]
77. Jeremić, D.; Andjelković, L.; Milenković, M.R.; Šuljagić, M.; Šumar Ristović, M.; Ostojić, S.; Nikolić, A.S.; Vulić, P.; Brčeski, I.; Pavlović, V. One-Pot Combustion Synthesis of Nickel Oxide and Hematite: From Simple Coordination Compounds to High Purity Metal Oxide Nanoparticles. *Sci. Sinter.* **2020**, *52*, 481–490. [CrossRef]
78. Barakat, A.; Al-Noaimi, M.; Suleiman, M.; Aldwayyan, A.S.; Hammouti, B.; Hadda, T.B.; Haddad, S.F.; Boshaala, A.; Warad, I. One Step Synthesis of NiO Nanoparticles via Solid-State Thermal Decomposition at Low-Temperature of Novel Aqua(2,9-dimethyl-1,10-phenanthroline)$NiCl_2$ Complex. *Int. J. Mol. Sci.* **2013**, *14*, 23941–23954. [CrossRef]
79. Zhou, W.; Wu, S.; Xu, Y.; Wang, X.; Liu, X. Characterization and Growth Mechanism of One-Dimensional NiO Nanostructures. *Chem. Phys. Lett.* **2002**, *364*, 428–434.
80. Ahmad, W.; Kaur, N. Microwave-Assisted Single Step Green Synthesis of NiO Nanoparticles Using Coleus Scutellariodes Leaf Extract for the Photocatalytic Degradation of Rufloxacin. *MRS Adv.* **2023**, *8*, 835–842. [CrossRef]
81. Salleh, N.A.; Mohammad, A.H.; Zakaria, Z.; Deghfel, B.; Yaakob, M.K.; Rahiman, W.; Kheawhom, S.; Mohamad, A.A. Microwave Assisted Synthesis of Nickel Oxide Nanoparticles at Different PH via Sol Gel Method: Experimental and First-Principles Investigations. *Inorg. Chem. Commun.* **2024**, *164*, 112415. [CrossRef]
82. Sabouri, Z.; Akbari, A.; Hosseini, H.A.; Darroudi, M. Facile Green Synthesis of NiO Nanoparticles and Investigation of Dye Degradation and Cytotoxicity Effects. *J. Mol. Struct.* **2018**, *1173*, 931–936. [CrossRef]
83. Gan, Y.X.; Jayatissa, A.H.; Yu, Z.; Chen, X.; Li, M. Hydrothermal Synthesis of Nanomaterials. *J. Nanomater.* **2020**, *2020*, 8917013. [CrossRef]
84. Gandhi, A.C.; Lin, J.G. Magnetic Resonance Study of Exchange-Biased Ni/NiO Nanoparticles. *J. Phys. Condens. Matter* **2017**, *29*, 215802. [CrossRef] [PubMed]
85. Gandhi, A.C.; Lin, J.G. Exchange Bias in Finite Sized NiO Nanoparticles with Ni Clusters. *J. Magn. Magn. Mater.* **2017**, *424*, 221–225. [CrossRef]
86. Navas, D.; Fuentes, S.; Castro-Alvarez, A.; Chavez-Angel, E. Review on Sol-Gel Synthesis of Perovskite and Oxide Nano-materials. *Gels* **2021**, *7*, 275. [CrossRef] [PubMed]
87. Han, D.Y.; Yang, H.Y.; Shen, C.B.; Zhou, X.; Wang, F.H. Synthesis and Size Control of NiO Nanoparticles by Water-in-Oil Microemulsion. *Powder Technol.* **2004**, *147*, 113–116. [CrossRef]
88. Du, Y.; Wang, W.; Li, X.; Zhao, J.; Ma, J.; Liu, Y.; Lu, G. Preparation of NiO Nanoparticles in Microemulsion and Its Gas Sensing Performance. *Mater. Lett.* **2012**, *68*, 168–170. [CrossRef]
89. Palanisamy, P.; Raichur, A.M. Synthesis of NiO Nanoparticles by Water-in-oil Microemulsion Technique. *Int. Res. J. Pure Appl. Chem.* **2014**, *4*, 494–506. [CrossRef]
90. Rinaldi-Montes, N.; Gorria, P.; Martínez-Blanco, D.; Fuertes, A.B.; Fernández Barquín, L.; Rodríguez Fernández, J.; De Pedro, I.; Fdez-Gubieda, M.L.; Alonso, J.; Olivi, L.; et al. Interplay between Microstructure and Magnetism in NiO Nanoparticles: Breakdown of the Antiferromagnetic Order. *Nanoscale* **2014**, *6*, 457–465. [CrossRef] [PubMed]
91. Issa, B.; Obaidat, I.M.; Albiss, B.A.; Haik, Y. Magnetic Nanoparticles: Surface Effects and Properties Related to Biomedicine Applications. *Int. J. Mol. Sci.* **2013**, *14*, 21266–21305. [CrossRef] [PubMed]
92. Wesselinowa, J.M. Size and Anisotropy Effects on Magnetic Properties of Antiferromagnetic Nanoparticles. *J. Magn. Magn. Mater.* **2010**, *322*, 234–237. [CrossRef]
93. Shim, H.; Dutta, P.; Seehra, M.S.; Bonevich, J. Size Dependence of the Blocking Temperatures and Electron Magnetic Resonance Spectra in NiO Nanoparticles. *Solid State Commun.* **2008**, *145*, 192–196. [CrossRef]
94. Rinaldi-Montes, N.; Gorria, P.; Martínez-Blanco, D.; Fuertes, A.B.; Barquín, L.F.; Puente-Orench, I.; Blanco, J.A. Scrutinizing the Role of Size Reduction on the Exchange Bias and Dynamic Magnetic Behavior in NiO Nanoparticles. *Nanotechnology* **2015**, *26*, 305705. [CrossRef] [PubMed]

95. Liu, D.; Li, D.; Yang, D. Size-Dependent Magnetic Properties of Branchlike Nickel Oxide Nanocrystals. *AIP Adv.* **2017**, *7*, 015028. [CrossRef]
96. Al Chaghouri, H.; Tuna, F.; Santhosh, P.N.; Thomas, P.J. Tiny Ni-NiO Nanocrystals with Exchange Bias Induced Room Temperature Ferromagnetism. *Solid State Commun.* **2016**, *230*, 11–15. [CrossRef]